energies

MDPI

Review

Recent Progress in Transparent Conductive Materials for Photovoltaics

Sandeep Kumar Maurya [1,*,†], Hazel Rose Galvan [2], Gaurav Gautam [3] and Xiaojie Xu [2,*,†]

[1] Department of Energy Science and Engineering, Indian Institute of Technology Bombay, Mumbai 400076, India
[2] Lawrence Livermore National Laboratory, 7000 East Avenue, Livermore, CA 94550, USA
[3] Department of Metallurgical and Materials Engineering, Indian Institute of Technology Roorkee, Roorkee 247667, India
* Correspondence: sandeepiitb22@gmail.com (S.K.M.); xu17@llnl.gov (X.X.); Tel.: +91-91370-38216 (S.K.M.)
† These authors contributed equally to this work.

Abstract: Transparent conducting materials (TCMs) are essential components for a variety of optoelectronic devices, such as photovoltaics, displays and touch screens. In recent years, extensive efforts have been made to develop TCMs with both high electrical conductivity and optical transmittance. Based on material types, they can be mainly categorized into the following classes: metal oxides, metal nanowire networks, carbon-material-based TCMs (graphene and carbon nanotube networks) and conjugated conductive polymers (PEDOT:PSS). This review will discuss the fundamental electrical and optical properties, typical fabrication methods and the applications in solar cells for each class of TCMs and highlight the current challenges and potential future research directions.

Keywords: transparent conducting materials; solar cells; optoelectronics; semiconductors; photovoltaics; graphene; carbon nanotube; metal nanowire network

Citation: Maurya, S.K.; Galvan, H.R.; Gautam, G.; Xu, X. Recent Progress in Transparent Conductive Materials for Photovoltaics. *Energies* **2022**, *15*, 8698. https://doi.org/10.3390/en15228698

Academic Editor: Alon Kuperman

Received: 31 October 2022
Accepted: 16 November 2022
Published: 19 November 2022

1. Introduction

Transparent conducting materials (TCMs) are a unique class of materials that exhibit excellent optical transmission in the visible light spectrum coupled with very high conductivity at room temperature. Materials such as metals that show high conductivity at room temperature remain opaque in the visible range. On the other hand, materials such as glass and intrinsic metal oxides/sulfides (ZnO, ZnS, CdO, SnO_2) show excellent transmittance in the visible light range but exhibit insulating behaviour at room temperature.

It is quite difficult to synthesize a material which retains transparency while becoming electrically conductive. In general, a wide bandgap (E_g > 3 eV) insulator is selected as a host material and modification in its electronic structure is realized from the numerous lattice defects to obtain conductivity. These defects are electrons and positive holes, excitons, vacant lattice sites/interstitial atoms, impurity in interstitial or substitutional positions, dislocations and stacking faults. Modification of the electronic structure with vacancies, substitutional and interstitial site defects by aliovalent doping plays a very important role in determining the conductivity. Understanding the effect of these defects led to the realization of TCMs.

Another common concept for realizing a TCM is ultra-thin metal films (UTMFs). To synthesize UTMFs, metal films can be made transparent by thinning down to a nm scale, but their sheet resistivity increases significantly as compared to the bulk material. When the electron mean free path is of the order of the film thickness, additional scattering at the surface causes a significant increase in the sheet resistance [1]. Scattering at the grain boundary in polycrystalline films also contributes to increasing the sheet resistance of the thin metal films [2]. Due to these shortcomings, UTMFs can not be effectively utilized as transparent conductors. More recent research studies focus on enhancing the performance of a TCM by understanding the microscopic nature of conducting the process in order to

analyze the role of morphology, crystal structure, and bonding on charge transport. After the realization of these types of materials, a large amount of research and development has been going on to make them more conductive as well as transparent in order to commercialize them.

There exist a wide range of TCMs such as ITO, doped ZnO (Al:ZnO, In:ZnO, Ga:ZnO), F-doped SnO_2 (FTO) and amorphous $InGaZnO_4$ (IGZO) for today's optoelectronic applications [3–9]. Extensive work has been carried out to find new alternative materials for TCMs, in particular, to replace existing TCMs and to explore viable *p*-type TCM. Additionally, a significant amount of work is being conducted on metal nanowire meshes, carbon nanotubes (CNTs) and graphene for TCM applications [10–13]. A uniform and conformal thin film deposited at low temperatures is essential for TCMs. Several vacuum and non-vacuum approaches such as sputtering, pulsed laser deposition (PLD), atomic layer deposition (ALD), chemical bath deposition (CBD), spray pyrolysis, spin coating and thermal evaporation can be used to obtain high-quality thin films. Deposition parameters and film composition (doping or alloying) play a vital role in determining the optical as well as electrical properties of the TCMs. Optimization of these parameters can lead to a high-performance TCM.

While metal oxide-based TCMs are widely used in photovoltaics, owing to their high conductivity and transparency, the scarcity of the raw materials, high cost of vapour deposition techniques and mechanical brittleness drive researchers to look for alternative transparent electrodes [5,13,14]. That is, TCMs have comparable electrical and optical properties but can be potentially made from earth-abundant materials by scalable low-cost fabrication methods. Metal nanowire network (MNWN)-based transparent electrodes have thus attracted great attention due to the intrinsic high conductivity, tunable transparency and solution-based deposition methods [15–17]. Furthermore, the mechanical flexibility of MNWNs may open up new opportunities for the development of unconventional photovoltaics, including semitransparent solar cells and flexible solar cells [15].

Poly(3,4-ethylenedioxythiophene):polystyrene sulfonate (PEDOT:PSS) is a conductive polymer which consists of positively charged conductive PEDOT and negatively charged insulating PSS [18]. PSS serves the purposes of charge balancing and dispersion in different solvents [19]. PEDOT:PSS has been widely used in optoelectronic devices as a hole transporting layer or a transparent electrode owing to its high and tunable conductivity (10^{-2}–10^{3} S cm^{-1}), transparency (∼90% with a film thickness of 100 nm), good film quality (roughness ∼5 nm), scalability (solution processable), high mechanical flexibility and air stability [18,20–22].

One of the goals in the development and research of emerging thin-film solar cells is to produce the most energy consumption from low-cost materials with high efficiencies and scalable fabrication processes [23–26]. More specifically, perovskite solar cells (PSCs) have emerged as a promising candidate with the use of lead halide perovskite (LHP) as the light harvester in solar cells [27–29]. The cubic cell unit of LHPs can be broken down into the following:

ABX_3 (general cubic cell unit)

$MABX_3$

$(CH_3NH_3)^+BX_3$

where MA = $(CH_3NH_3)^+$; B = Pb or Sn; X = Cl, Br or I.

Moreover, LHPs achieve a power conversion efficiency (PCE) as high as 31% [30]. In recent years, PSCs have received more attention in the photovoltaic community because of their low cost, tunable bandgap, high carrier mobilities and rapid improvement in their power conversion efficiency [30–32]. Studies show an impressive and high-power conversion efficiency of above 14.1% and up to 25.27 within a decade [23,26]. Unfortunately, metal electrodes (e.g., Au, Ag and Al), and transparent conducting oxides (TCOs) (e.g., indium tin oxide (ITO), indium zinc oxide (IZO)) used in PSCs have high costs due to the complex processing of TCOs and are limited in their commercial applications due to the limited supply of metals (e.g., indium) [32,33]. Additionally, the perovskite material degrades in

the presence of water, which leads to the formation of hydrated phases $CH_3NH_3PbI_3 \cdot H_2O$ and $(CH_3NH_3)_4PbI_6 \cdot 2H_2O$ [34].

Moreover, metal-based electrodes such as Al, Ag and Au are not ideal materials in the long run due to the finite supply of them. Al is easily oxidized in air, which causes a dramatic decrease in conductivity. Ag is not stable due to the formation of an Ag-halide that degrades device performance [35,36]. Similarly, Au also reacts with halides (iodide) ions, has high reflectivity and is expensive [35,37]. Additionally, TCOs have been employed in standard PSCs as well as flexible perovskite solar cells (FPSCs) due to the low-temperature fabrication process, chemical stability, high optical transparency, low sheet resistance and established mass production process [35,38]. However, ITO is rigid and brittle. This will likely result in breakage and degradation of the devices under mechanical deformations for flexible device applications. Indium is also scarce, and the costly fabrication process (e.g., vacuum deposition techniques such as sputtering and pulsed laser deposition) makes it the most expensive component in PSCs/FPSCs; it comprises 50–60% of the total material cost [24,38,39]. An alternative to the high cost and limited supply of metallic electrodes and TCMs is to use carbon-based materials to replace standard electrodes. This is largely beneficial because carbon is a common organic material that is abundantly available on earth. It is known for its electrochemical activity and conductivity, resistance to water and flexibility when processed [39].

2. Physics of TCMs

TCMs have to be optically passive and favourably transparent. Figure 1 shows electromagnetic spectrum with favourable transmission window for TCMs.

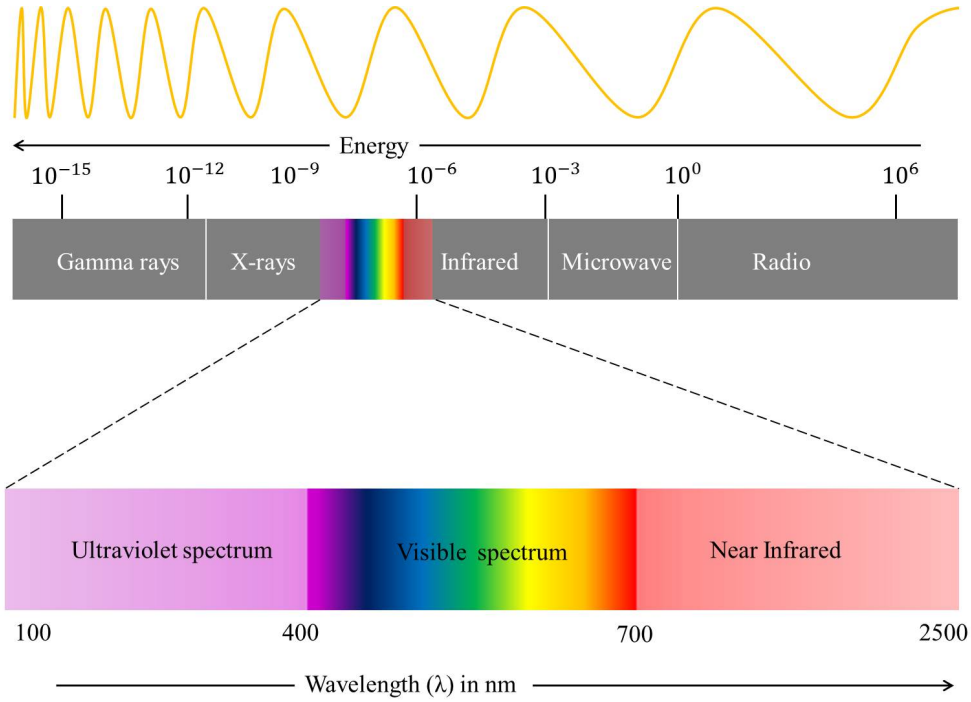

Figure 1. Electromagnetic spectrum according to energy along with ideal transmission window for TCMs.

Knowledge of classical and quantum descriptions of solid-state materials is required to understand the carrier transport mechanism in transparent conducting films. The infrared reflectance part can be perfectly described using the classical electron sea analogy, whereas band-to-band absorbance in the UV can be explained through the quantum description. These materials are transparent due to their wide band gap ($E_g > 3$ eV) and conducting due to excessive doping ($\sim 10^{21}$ cm^{-3}). Carrier transport in these materials can be understood

easily if we treat them as metals having plasma frequency in the IR range and transparent in the visible range.

In 1924, H. Mott-Smith derived the accurate formula for the characteristic plasma frequency [40–42]

$$\omega_p = \sqrt{\frac{4\pi n e^2}{m}}, \tag{1}$$

where n is the carrier density, e is the charge of an electron and m is the mass of an electron. This frequency represents the most fundamental parameter of plasma. This frequency acts as a filter for all electromagnetic waves. Electromagnetic waves with a lower frequency than plasma frequency will not be able to pass through.

Drude theory helps in further understanding of plasma frequency which is highly useful in improving the electrical and optical properties of TCMs. The plasma dielectric function is given by the Drude formula [43]

$$\epsilon(\omega)_p = 1 - \frac{\omega_p^2}{\omega^2}, \tag{2}$$

this formula can be combined with transverse wave propagating through uniform medium [41,42]

$$\omega = \frac{kc}{\sqrt{\epsilon(\omega)}}, \tag{3}$$

gives

$$\omega^2 = \omega_p^2 + c^2k^2, \tag{4}$$

where c is the speed of light and k the wavevector. This is the dispersion relation of a transverse mode that can propagate through the transverse bulk plasmon. Figure 2 clearly shows that no other modes can propagate through the medium with frequencies less than the plasma frequency.

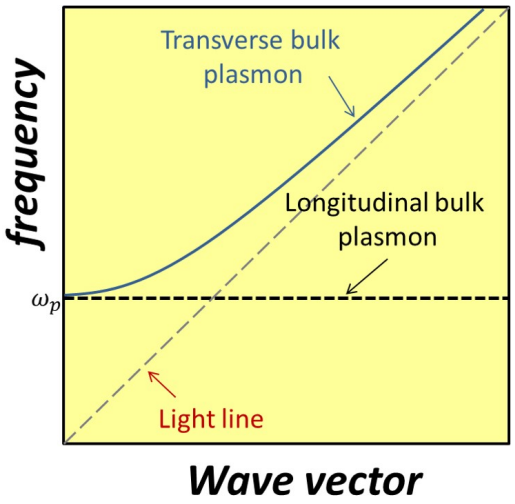

Figure 2. Photon and plasmon dispersion.

This theory suggests that films fabricated with either higher or lower permittivity can have varying optical properties. This will provide an advantage in fabricating devices such as organic light emitting diodes (LEDs) and solar cells, where the work function of TCMs plays critical role in device performance.

The second requirement of TCM is its high conductivity, as presented below

$$\sigma = ne\mu, \tag{5}$$

where μ is the carrier mobility. Now combining Equations (1) and (5) gives following

relation

$$\sigma = \frac{\omega_p^2 \mu m}{4\pi e}, \tag{6}$$

From the equation it is quite evident that the high conductivity in a TCM can be obtained first by setting plasma frequency $\omega_p = \omega_{pmax}$, and increasing mobility (μ). Equation (6) can be re-written in terms of sheet resistance (R_{sh}) as following

$$\omega_p = 2\sqrt{\frac{\pi e}{m\mu t}} R_{sh}^{-1/2}, \tag{7}$$

where t is the film thickness.

Increasing the conductivity from 100 Ω-sq^{-1} to 5 Ω-sq^{-1} results in a transmittance drop in the near-infrared (NIR) range. This is primarily due to free electrons changing the infrared plasma frequency. Additionally, in order to achieve n-type conductivity in wide-band gap metal oxides, the material should have a relatively high electron affinity and low CBM. For example, SnO_2 with a band gap of ∼3.6 eV and electron affinity of ≈4.8 eV would be an excellent candidate for fabricating a TCM [3,44,45]. On the other hand, HfO_2 with a wide band gap of 6 eV and electron affinity of only 2.5 eV will not be a suitable material for TCM. Further, in oxide semiconductors, this gives an assertion that the deficiency of oxygen in certain metal oxides can induce a shallow defect level near CBM that leads to *n*-type conductivity at room temperature.

3. Transparent Conducting Materials

TCMs are an integral part of solar cells and are used as hole transport and electron transport layers along with a window to allow light through to the PV absorber layer, as shown in Figure 3. The TCMs are generally used as an interfacial layer to improve the contact resistance between the PV absorber layer and a metallic reflector, improving the refractive index matching. The high conversion efficiency in solar cells such as microcrystalline, Si, perovskite, CIGS, CZTS and various multi-junction requires minimal sheet resistance of $\leq$10 Ω sq^{-1} and transparency $>$ 80% of TCMs in wide spectrum range (400–1300 nm). The following sections will outline all possible TCMs that can be used as a hole transport layer (HTL), electron transport layer (ETL) and back contact in solar cells.

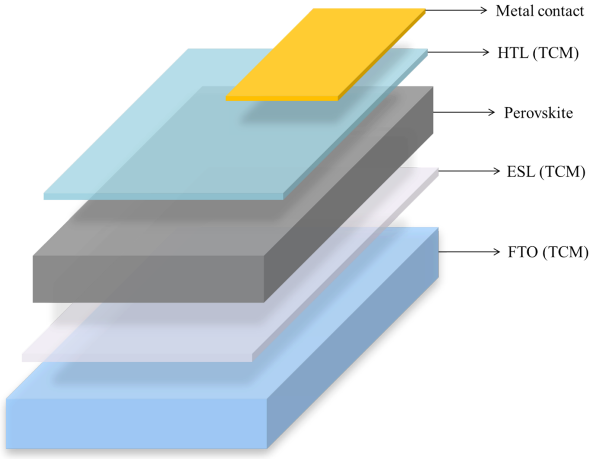

Figure 3. A typical schematic of a solar cell using both n- and p-type TCMs. The cells consist of metal contacts, a hole transport layer (HTL), an absorber layer, and an electron transport layer (ETL).

3.1. n-Type Transparent Conductors

Initially, *n*-type TCMs were developed by oxidation of thin metal films in a reactive atmosphere (O_2 and Ar). The metal thin films were deposited via evaporation and DC sputtering [46]. The resistivity of thin films, fabricated by oxidation of thin metal films,

was significantly high compared to bulk materials. This was because the electron mean free path was of the order of film thickness, also scattering at the grain boundaries in the polycrystalline film plays a major role in reducing the conductivity of the film [1]. These two major effects limited the conductivity in thin polycrystalline films [2]. Other methods to deposit TCMs were via spraying or dipping. After the early discovery of TCMs, significant improvement in the performance has been reported in a number of binary, secondary, ternary and quaternary compounds (metal oxides). These reported metal oxide compounds show appreciable conductivities and good transmission in the visible light spectrum but conductivity in these films is still quite low compared to that of metals. In order to facilitate *n*-type conductivity in metal oxides, various lattice defects such as oxygen vacancies ($V_O^{\bullet\bullet}$), cation interstitials and different substitutional defects have been introduced to effectively create shallow defect sites near conduction band minima. Moreover, some metal oxides such as ZnO are naturally *n*-type in nature due to the presence of different defects. The presence of these defect levels helps electrons to directly inject into the conduction band from nearby defect donor levels. Further increase in doping leads to the delocalization of electrons from defects sites such that the electronic state at the CBM becomes filled resulting in a shift in the Fermi level above the CBM. This phenomenon is known as the Burstein–Moss shift, which effectively increases the optical band gap of the material. The band theory of solids provided an explanation of doping in semiconductors and an understanding of the properties of such oxide materials.

The first *n*-type TCM was investigated by Badeker in 1907. He fabricated cadmium oxide (CdO) via incomplete thermal oxidation (in air) of a sputtered Cd metal thin film and reported a resistivity as low as 1.2×10^{-3} Ω cm. Further, various *n*-type TCMs were fabricated, patented and commercialized in the early 1940s. An example of an SnO_2-based *n*-type TCM was developed and patented in the 1930s for its use as an airplane windshield de-icer. The best-known TCM to date, *n*-type Sn-doped indium oxide (ITO), was also developed and patented by USA based company named Corning in 1951. ITO has been the most important part of the TCM industry to date. High-performing ITO films have been developed via physical vapour deposition (PVD), atomic layer deposition (ALD), chemical vapour deposition (CVD), spray pyrolysis, spin coating, sol–gel method, molecular beam epitaxy (MBE), etc. [47]. The reported minimum resistivity of impurity-doped In_2O_3 has been unchanged for more than 40 years, which is 1–2 $\times 10^{-4}$ Ω cm.

In the late 1970s, CdO was further investigated for its application as a *n*-type TCM. CdO and CdO-based ternary compounds (Cd_2SnO_4 CTO) have shown to be good TCMs with excellent transparency in the visible light range and resistivity <10^{-4} Ω cm at room temperature. However, CTO couldn't be used as a TCM due to the presence of toxic Cd and high processing temperature (>600 °C). Additionally, it is quite difficult to achieve a single-phase material with a CdO-based compound [48–50]. CdO- based TCMs are very favourable to be used in II–VI compounds (CdTe and Cd(S, Te)).

Successful development of high conducting oxygen-deficient ZnO and SnO_2, doped Zn/Sn oxides (M:Zn/Sn-O where M: Al, B, Ga, In, F, Sb, Ta, P) and ternary metal oxide compounds ($ZnSnO_3$, Zn_2SnO_4, $Zn_mIn_2O_{3+m}$; m = 2−7, $MgIn_2O_4$, $GaInO_3$, $(GaIn)_2O_3$, $In_4Sn_3O_{12}$) with excellent transparency in visible light range expands the horizon of applicability of TCMs in various optoelectronic devices [51,52]. These materials also showed conductivities >5000 S cm^{-1} with mobilities of more than 30 $cm^2V^{-1}s^{-1}$. Further, multi-component oxides such as ZnO-SnO_2 and ZnO-In_2O_3 were extensively studied for their potential application in thin film solar cell devices. SnO_2 and ZnO-based TCMs are frequently used in compound semiconductors of the III-V type compounds (GaAs, (Al,Ga)As, InP and (In,Ga)P). Figure 4 shows some of the best known *n*-type TCMs reported to date. Table 1 shows most of the *n*-type TCMs with deposition methods and optoelectronic properties.

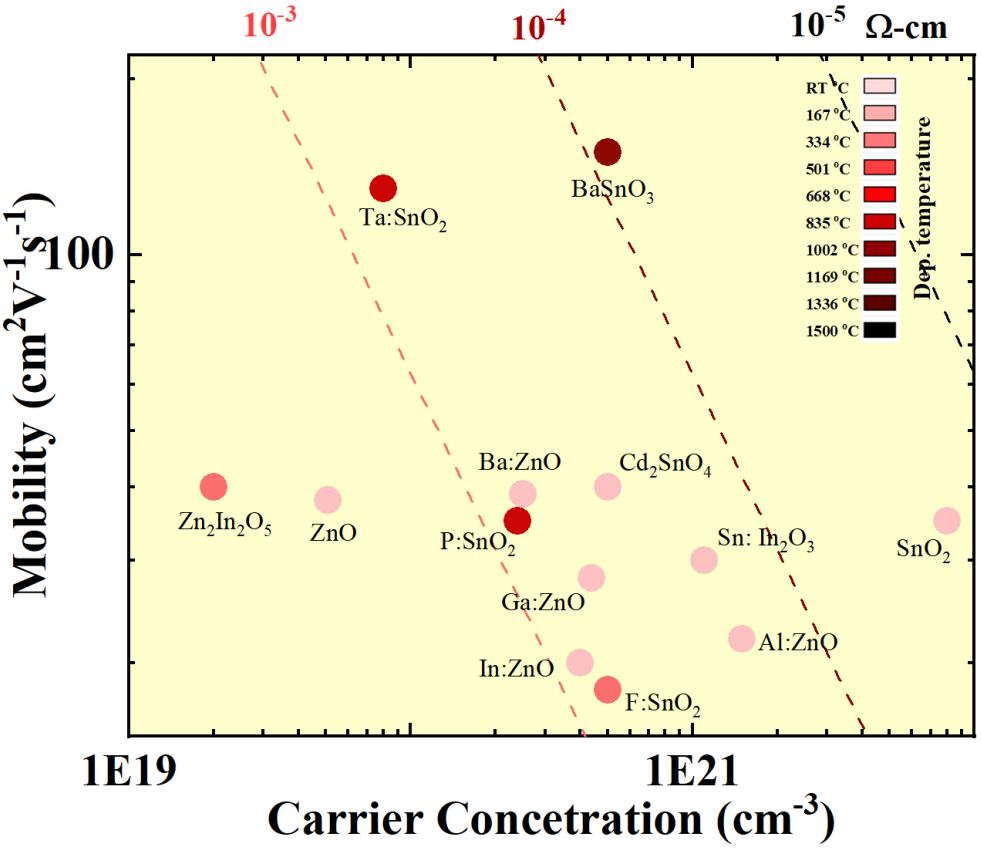

Figure 4. Mobility is plotted against carrier concentration for the highest performing *n*-type TCMs. Datapoints present the obtained mobility for the corresponding carrier concentration. The colour of the circles signifies the deposition temperature of the film. Dotted lines represent the line of equal resistivity.

Table 1. List of some *n*-type TCMs with deposition methods and optoelectronic properties.

Material	Deposition Method	Deposition Temperature	Rsh (Ω/□)	σ (S cm^{-1})	μ (cm^{2}V^{-1}s^{-1})	n (cm^{-3})	Average Optical Transmisson	Thickness (nm)
Sn:In_2O_3 [47]	EBE	~150	<20	>5000	30	1.1×10^{21}	>85%	300
ZnO [51]	Sputter	~150	<20	>500	38	5.1×10^{19}	>85%	550
Al:ZnO [51]	Sputter	~150	<20	>5000	22	1.5×10^{21}	>85%	425
B:ZnO [51]	Sputter	~150	<20	>1500	39	2.5×10^{20}	>85%	595
Ga:ZnO [51]	Sputter	~150	<20	>2000	28	4.4×10^{20}	>85%	500
In:ZnO [51]	Sputter	~150	<20	>1200	20	4.0×10^{20}	>85%	650
SnO_2 [53]	SP	450	<20	>800	>30	8×10^{21}	>80%	720
F:SnO_2 [54]	SP	380	<20	>1000	18	5×10^{20}	>80%	210
P:SnO_2 [55]	CVD	550	<20	>1500	35	2.4×10^{20}	>80%	400
Sb:SnO_2 [56]	Sol-gel	350	<10	>10000	–	–	>60%	340
Ta:SnO_2 [57]	PLD	600	<20	>1500	130	8×10^{19}	–	120
$Zn_2In_2O_5$ [52]	Sputter	350	<20	>2500	>30	5×10^{20}	>80%	~400
Cd_2SnO_4 [48]	Sputter	>150	<20	>5000	>30	$>1 \times 10^{19}$	>80%	1000
$BaSnO_3$ [58]	MBE	>1230	<20	>5000	150	$>4 \times 10^{20}$	–	31

In laser lithography and high-efficiency solar cell fabrication, new ultraviolet transparent conducting materials will be required since in the process of laser lithography, elector-conductive materials are necessary, which transmit the UV light at <250 nm. Additionally, in most of the available solar cells, the used transparent conductor has a band gap <4 eV, which leads to the elimination of photons in the UV range. The solar cell efficiency can be increased significantly if high-energy photons are utilized in power conversion. Wide band gap Ga_2O_3 (>4 eV) had been studied for its potential application in solar cells

and lasers. β-Ga_2O_3 has shown conductivity ~30 S cm^{-1} and transparency >80% in the visible light range at room temperature [59].

Wide band gap doped/un-doped ternary oxide with perovskite structured materials such as $BaSnO_3$ and $SrTiO_3$ have been studied for potential transparent conductor application [58,60]. $SrTiO_3$ has shown a mobility below 10 $cm^2V^{-1}s^{-1}$ and conductivity ≈500 S cm^{-1} at room temperature [61]. MBE-grown $BaSnO_3$ on $PrScO_3$ exhibited mobility ≈150 $cm^2V^{-1}s^{-1}$ with a carrier concentration of 7.2 × 10^{19} cm^{-3} [62]. Recently, La-doped $BaSnO_3$ grown on $SrTiO_3$ (001) substrate shows a room temperature carrier concentration of 4 × 10^{20} cm^{-3} with mobility of ≈150 $cm^2V^{-1}s^{-1}$ [58].

3.2. p-Type Transparent Conductors

As discussed in the last section, wide band gap oxide materials such as FTO, AZO and ITO are some of well known *n*-type TCMs and are widely used in optoelectronic devices such as LEDs, solar photovoltaics (PV), etc. However, the counterpart *p*-type TCMs are comparatively less investigated [63]. In general, *n*-type TCMs are metal oxides in nature. However, it is very challenging to fabricate oxide *p*-type TCMs as there are several fundamental complexities associated with it. The electronic structures of such metal oxides are one of the leading causes, as proposed by Kawazoe et al. [64]. The *p*-type metal oxides show strong localization behaviour of positive holes at the edge of VB. These localized state forms due to the ionicity of metallic oxide, resulting in strong localization of holes at oxygen *2p* levels, which is in the upper edge of VB. The strong localization arises due to non-stoichiometry or substitutional doping in the material. The localized oxygen *2p* levels help in the formation of deep acceptor defect levels, far from the valence orbit of metallic atoms. This gives rise to the localization of holes which results in poor conductivity and hole mobility as holes have to overcome large energy barriers in order to move in the crystal lattice. Kawazoe et al. proposed the modification of VB to overcome the shortcoming of deep localization of holes. It can be performed by mixing orbitals with suitable cations that have enough filled energy level comparable to the oxygen *2p* level [64]. To reduce the strong localization of holes in oxygen ions due to high electronegativity of oxygen, modulation of the top of the valence band was performed by chemical bonds between oxygen $2p^6$ and Cu $3d^10$ orbitals. This particular method is called "chemical modulation of the valence band (CMVB)" [63]. Additionally, higher effective mass of holes ($m_e < m_h$) in metal oxide compounds also contributes in lowering overall mobility of the material [65]. Additionally, it is desirable that the materials contain highly electropositive ions to shift conduction band towards high energy levels.

The first *p*-type transparent conductor, $CuAlO_2$ crystallizing in the delafossite structure, was reported in 1997 by Kawazoe et al. and possessws a hole conductivity of ≈1 S cm^{-1} with carrier concentration of 1.3 × 10^{17} cm^{-3} and hall mobility of the positive holes of 10.4 $cm^2V^{-1}s^{-1}$ at room temperature [66]. Cation vacancy and interstitial oxygen lead to excess oxygen in the $CuAlO_2$ delafossite phase, resulting in p-type conductivity. These films were developed via solid-state reaction process at 700 °C in an oxygen-rich environment. Elevated processing temperature and poor optoelectric properties limited the application of $CuAlO_2$ in different optoelectronic devices. Further, several CuM_xO_2 (where $M = Cr, Sc, Y, Fe, Co, Rh, Ga, Ca, Mg$, etc.) compounds isostructural with $CuAlO_2$ were studied for a potential *p*-type transparent conductor [67–70]. Initial reports of delafossite $CuScO_2$, $CuGaO_2$ and $CuY_{1-x}Ca_xO_2$ films showed conductivity in the range of 5 to 30 S cm^{-1} with mobility ≤10 $cm^2V^{-1}s^{-1}$ [64,67,71]. The mobilities in these films are quite low since the valence band consist of oxygen *2p* bands as lattice relaxation around holes strongly traps the potential carriers. To achieve higher mobility, the valence band should consist of cation *d* or *s* band instead of oxygen *2p* bands. Later studies on delafossite structure were focused on $CuCrO_2$ based compounds as *d-d* transitions possibly resulted in higher mobility. One such film, $CuCr_{1-x}Mg_xO_2$, showed conductivity >200 S cm^{-1} and mobility >10 $cm^2V^{-1}s^{-1}$. However, the overall transparency in the visible light range was still <50% [70]. Table 2 shows most of the *p*-type TCMs with deposition methods and optoelectronic properties.

The idea of band modulation is not limited only to oxide materials. Other chalcogenides (sulphides in particular) and mixed chalcogenides (O, S, Se combined) were also reported for their excellent optoelectronic properties to be used as *p*-type TCMs. Among all, oxysulphides and sulphides are the most superior compounds due to their transparency in the visible light region. The inclusion of any alkali and rare earth ions also showed moderate dispersion at the top of the valence band resulting in better transparency. Ueda et al. reported one such layered oxysulphide (Sr-doped LaCuOS), which showed excellent transparency in visible light range but conductivity remained ≈0.3 S cm^{-1} at room temperature [72]. Further, Hiramatsu et al. reported elevated carrier concentration (10^{21} cm^{-3}) with hole mobility of ≈10 $cm^2V^{-1}s^{-1}$ in layered Mg-doped LaCuOSe [73]. Further, several sulphide and iodide compounds such as $CuAl_{1-x}Zn_xS_y$, $BaCu_2S_2$, $Cu_xZn_{1-x}S$, $(CuS)_x(ZnS)_{1-x}$, CuI and I-doped CuI were reported to have excellent conductivity and transparency [74–82]. Reported Cu-Zn-S and CuI compounds were fabricated either at room temperature or at temperature < 100 °C. Low deposition temperatures and the use of Earth-abundant elements in these compounds make them cost-effective as well as compatible to be used in many device applications. To date, Cu-based sulphide and iodide compounds are some of the best performing *p*-type TCMs. Recently, sputtered $Cu_xZn_{1-x}S$ have been successfully used as a hole selective back contact for poly-crystalline CdTe solar cells (Glass/FTO/Cd(S,O)/CdTe/$Cu_xZn_{1-x}S$/Au) [83]. Figure 5 shows a number of commonly known *p*-type TCMs. These TCMs have been presented in the figure by plotting the conductivity of the films against deposition temperature. Secondary information has been added as a transmission for the films in the visible light range (at ≈550 nm). Different films with similar conductivities show varying transmissions, suggesting the varying performance of TCMs. This interactive figure helps us to identify better TCM, which can be deposited at lower temperatures and has higher conductivity with a fair transmission in the visible light spectrum. Further, from Figure 5 we can observe that most of the *p*-type TCMs are fabricated at high temperatures (>400 °C). The doped and undoped Cu-based compounds constitute the typical materials that have been studied. These materials show good transmittance in the visible light range but show low hole mobility [65]. However, some non-oxide chalcogenide-based *p*-type transparent conductors such as Zn-doped $CuAlS_2$ [84] and undoped α-$BaCu_2S_2$ [85] show transmittance >80% and higher hole mobility with appreciable conductivity of ≈64 S cm^{-1} and 17 S cm^{-1}, respectively.

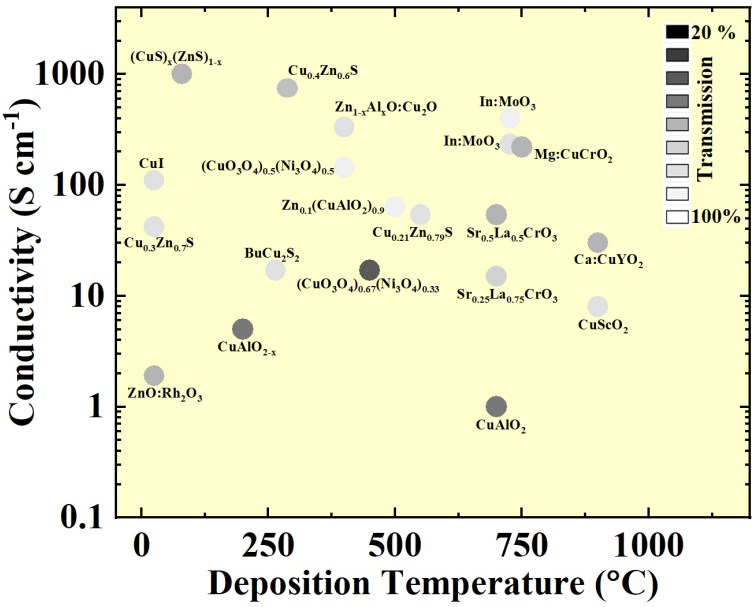

Figure 5. Conductivity plotted against maximum processing temperature for the highest performing *p*-type TCMs. Datapoints present in the plot give the value of maximum conductivity achieved at a given synthesis temperature. The colours of the circles represent the transmission reported at 550 nm.

Table 2. List of most of the *p*-type transparent conductors.

Material	Deposition Method	Deposition Temperature	Rsh (Ω/□)	σ (S cm^{-1})	μ (cm^{2}V^{-1}s^{-1})	n (cm^{-3})	Average Optical Transmisson	Thickness (nm)
$BaCu_2S_2$ [85]	Sputter	264	1400	17	3.3	1×10^{19}	~50%	430
$Ba_{0.9}K_{0.1}CuSF$ [86]	SSR	650	na	82	na	na	na	na
$CuAlO_2$ [66]	Furnace	700	2×10^5	1	10.4	1.3×10^{17}	~35%	~500
$CuAlO_{2-x}$ [63]	Sputter	200	10×10^5	5	~24	1.2×10^{18}	~35%	500
$Cu_{0.95}Pt_{0.05}FeO_2$ [87]	SSR	1050	na	12.5	1.8	4.04×10^{19}	na	na
$CuScO_2$ [67]	Sputter	900	~3030	30	na	na	~40%	110
Ca:$CuYO_2$ [88]	Sputter	900	10,500	8	na	na	55%	~120
$CuAl_{0.9}Zn_{0.1}S_2$ [84]	CSA	500	~1570	63.5	na	6.9×10^{19}	~85%	~100
$Cu_{0.21}Zn_{0.79}S$ [77]	PLD	550	1085	54	0.7–2.0	$1–5 \times 10^{20}$	~60%	100
$Cu_{0.3}Zn_{0.7}S$ [80]	PLD	RT	1090	42	0.2–1.0	$0.3–1.1 \times 10^{20}$	~50%	218
$(CuS)_x(ZnS)_{1-x}$ [78]	CBD	80	200	1000	0.5–2	$2–8 \times 10^{21}$	~50%	50
Cu:ZnS [81]	Sputter	350	49	752	0.5–1.6	6×10^{20}	~75%	200
CuI [89]	RTA	RT	na	110	4.1	1.70×10^{20}	~70	50–300
$(Co_3O_4)_{0.5}(Ni_3O_4)_{0.5}$ [90]	Sputter	400	300	333	na	na	15%	100
$(Co_3O_4)_{0.67}(Ni_3O_4)_{0.33}$ [91]	SC	450	6000	17	na	na	25%	100
In:MOo_3 [92]	Furnace	395	287	233	28.2	5.20×10^{19}	~70%	150
In:MOo_3 [92]	Furnace	435	313	400	11.9	2.10×10^{20}	84%	80
Mg:$CuCrO_2$ [69]	Sputter	750	~180	220	<1	na	35%	~250
$Mg_{0.2}La_{0.8}CuOSe$ [93]	RSPE	1000	~475	140	4	2.20×10^{20}	na	~150
$Sr_{0.25}La_{0.75}CrO_3$ [94]	MBE	700	8300	15	0.03	3.40×10^{21}	54%	80
$Sr_{0.5}La_{0.5}CrO_3$ [94]	MBE	700	3700	54	0.04	7.50×10^{21}	42%	50
(Ni, In):ZnO [95]	USP	450	~700	59	155	2.40×10^{18}	na	200–300
$Zn_{1-x}Al_xO:Cu_2O$ [96]	Sol-gel	400	175	144	27.8	2.0×10^{18}	85%	~400
ZnO:Rh_2O_3 [97]	Sputter	RT	17,500–50,000	1.9	na	na	45%	100–300
Zn-Co-O [98]	PLD	RT	~3500	21	~1	$\sim 1.3 \times 10^{20}$	na	100–200
$Cu_{1+x}Al_{1-x}S_2$ [99]	SPS	800	na	250	21.2	7.3×10^{19}	na	na

Figure 6 shows the carrier-concentration-to-mobility plot of some of the best-known *p*-type TCMs. The resistivity range shows that most of the *p*-type TCMs lie in below 10^{-2} Ω cm resistivity range and very few lie in range 10^{-2} to 10^{-3} Ω cm range. To date, most of the *p*-type TCMs have shown very poor conductivity at room temperature.

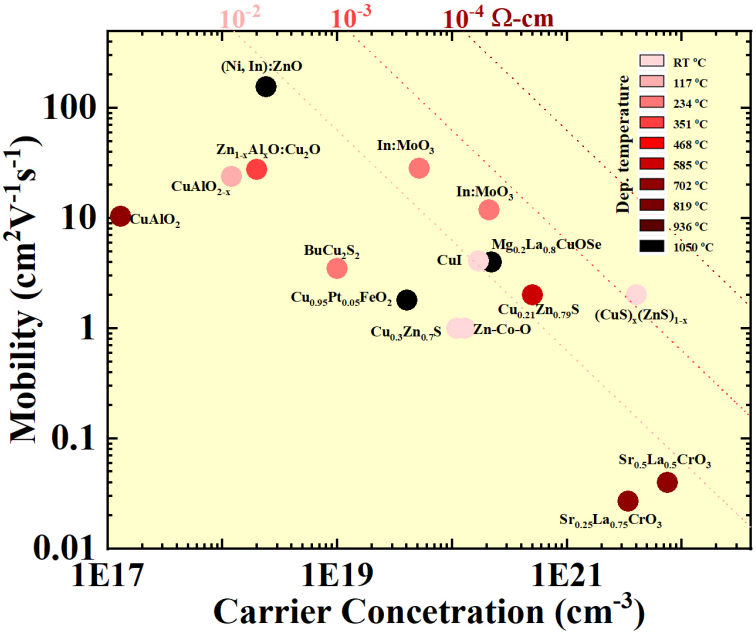

Figure 6. Mobility is plotted against carrier concentration for the highest performing *p*-type TCMs. Datapoints present the obtained mobility for the corresponding carrier concentration. The colour of the circles signifies the deposition temperature of the film. Dotted lines represent the line of equal resistivity.

3.3. Metal Nanowire-Based TCMs

A variety of metal nanowires have been developed for potential applications in transparent electrodes, such as silver (Ag), copper (Cu) and gold (Au) NWs [17]. Metal nanowires are typically synthesized by a solution-phase chemical synthesis route, which is to start with metal nuclei reduced from metal ions, grow into nanosized crystals with capping agents an-

chored on specific facets and eventually merge into an-isotropic assembly [100,101]. Factors such as aspect ratio (length/diameter) and capping agents play an important role in the conductivity and transmittance of MNWNs [15]. In general, a higher aspect ratio is favoured for higher conductivity and transmittance due to enhanced percolation conduction, fewer junctions, more void space and reduced light scattering [17]. The dimensions of metal NWs for TCMs reported in the literature typically range from a few to tens of nanometers in diameter and a few to hundreds of microns in length, with an average aspect ratio of 100–5000 [17,102]. The long insulating capping agents (such as PVP) from synthesis would dramatically hinder the conductivity of MNWNs, and thus need to be replaced with shorter capping agents such as inorganic salts (NaCl) [103,104].

A porous interconnected network is the most common form of MNWs applied as electrodes in optoelectronic devices. Various solution-processed methods have been exploited to assemble MNWNs from metal nanowires, including slot die coating, doctor blading, screen printing, ink-jet printing, spin coating, spray coating, dip coating, vacuum filtration, Mayer rod, electrospinning, etc. [16,17]. All these efforts are aimed to develop a low-temperature, low-cost saleable deposition method of high-performance robust MNWN electrodes.

There are a few key factors to evaluate the properties of MNWN electrodes: conductivity, transmittance and haze factor [15]. It is a trade-off between the conductivity and transmittance of an MNWN electrode [105]. Network density, the number of NWs per unit area, is a critical parameter to tune the overall electrical and optical properties of an MNWN electrode. A higher network density will typically increase its conductivity, owing to more conductive paths, however, it will reduce the transmittance as it blocks more photons from passing through [106,107]. The haze factor, defined as the amount of light scattered when light passes through a transparent sample (see equation below), is a critical parameter for light management [108].

$$Haze = \frac{Forward\ scattered\ light}{Forward\ scattered + Forward\ non\ scattered} \times 100\% \quad (8)$$

It is found that haze factor increases linearly with network density [109,110]. Therefore, the network density needs to be well balanced for conductivity, transmittance and haze factor. Contact resistance at the junctions is also an important factor that hinders the conductivity of the MNWNs [111]. Postprocessing treatment is typically employed to enhance its conductivity, such as annealing, mechanical pressing and nano-wielding [112–115].

Figure 7 shows a schematic illustration of design principles for MNW-based synthesis for application in solar cells. The standard solar cell architecture is substrate/bottom electrode/electron transporting layer (ETL)/photoactive layer/hole transporting layer (HTL)/top electrode [116,117]. The sun passes through the transparent electrode, which can either be the top electrode or the bottom electrode. Both electrodes are required to be transparent for a semitransparent solar cell.

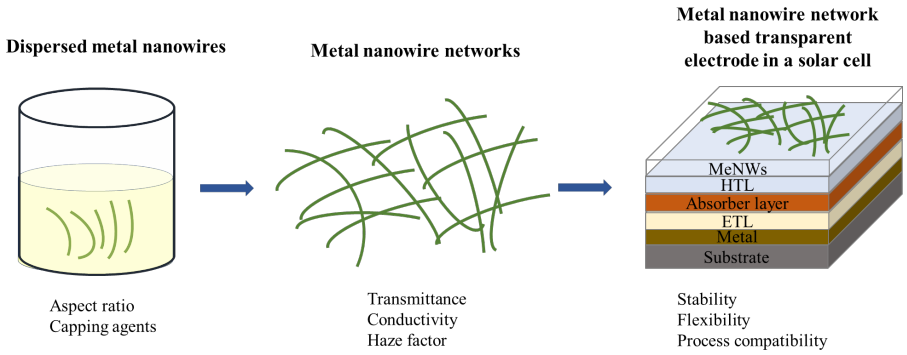

Figure 7. Schematic illustration of the design principles for metal nanowire network based transparent conductors: from the synthesis of metal nanowires, assembly of metal nanowire networks and applications in solar cells.

MNWNs have been considered one of the most promising transparent electrodes for organic photovoltaics (OPVs) [14]. Compared with vacuum-deposited metal oxide electrodes, MNWNs have comparable conductivity and transparency but are more compatible with the solution-processed low-cost high-throughput fabrication of OPVs [118,119]. A representative organic solar cell with metal nanowires as the transparent electrode has a device configuration of Ag NWs/PEDOT:PSS/P3HT:PCBM/Ca/Al [119]. Researchers explored different strategies to optimize the conductivity and transparency of Ag NW electrodes for a higher power conversion efficiency. With the increased J_{sc} and FF, the PCE of such devices was improved from ~1.8% to ~4.2% [119–123].

Semitransparent solar cells, which combine energy conversion and optical transparency in one device, have become a rising star in emerging photovoltaics [124]. As the two key features of a semitransparent solar cell, power conversion efficiency (PCE) and averaged visible transmittance (AVT) is generally used to evaluate its performance [125,126]. Owing to the same reasons as that in conventional OPVs, MNWNs are regarded as one of the most important transparent electrodes in semitransparent perovskite solar cells (PSCs). To maximize the visibility while preserving the efficiency of a cell, high conductivity and transmittance are desired for both the top and bottom electrodes. It was reported that Ag NW electrodes hardly deteriorated the transmittance of a cell in comparison with a metal thin-film transparent electrode [127]. A presentative semitransparent PSC configuration of ITO/PEDOT:PSS/perovskite/PC60BM/ZnO/Ag NWs was proposed by Guo et al., where a PCE of ~8.5% and AVT of ~28.4% was demonstrated [128]. Others tried to substitute the ETL and HTL with TiO_2 and spiro-OMeTAD to further improve the efficiency, where a PCE of ~11.07% and AVT of ~9% was achieved [129]. One of the challenges for employing MNWNs in PSCs is chemical stability as the halide tends to migrate from the active layer to react with the metal nanowires and form unstable halide compounds [130,131]. Various attempts have thus been made to introduce a buffer layer in-between to reduce chemical corrosion [129,132].

As another emerging direction in photovoltaics, flexible solar cells have attracted great attention in the past two decades due to their potential in portable and wearable applications [133,134]. Other than PCE, mechanical robustness is also an important feature for flexible solar cells, such as deformability under extreme/repeated conditions [135]. Considering the Young's modulus of the photoactive layers of different photovoltaics, quantum dot solar cells and perovskite solar cells are the two most promising types to realize the feature of flexibility [136–140]. In contrast to the brittle inorganic metal oxide electrodes, the intrinsic flexibility of MNWNs make them a good candidate as a transparent electrode for flexible solar cells.

There are two representative device architectures of flexible solar cells: planar and fibre-shaped. The former is constructed on a flexible substrate, such as polyethylene terephthalate (PET) and polyethylene naphthalate (PEN) [141], while the latter is built on a thin metal wire that serves as the substrate as well as the core electrode [142]. MNWNs are typically employed as the transparent electrode in the planar flexible SCs or the shell electrode in the fibre-shaped flexible SCs.

Despite the flexibility of MNWNs, there remain several issues with using MNWNs as the transparent electrode in flexible SCs, including high surface roughness and poor adhesion [143,144]. Composite TCMs are thus widely explored to overcome these challenges. For example, Bae et al. reported that the stability of MNWNs was greatly enhanced when introducing a thin ITO coating on the networks [132]. Similarly, the PEDOT:PSS/MNWN composite electrode was also explored in flexible SCs, where increased flexibility and mechanical stability was demonstrated [145,146]. Figure 8 shows a schematic illustration of conventional PV, semitransparent PV and flexible PV.

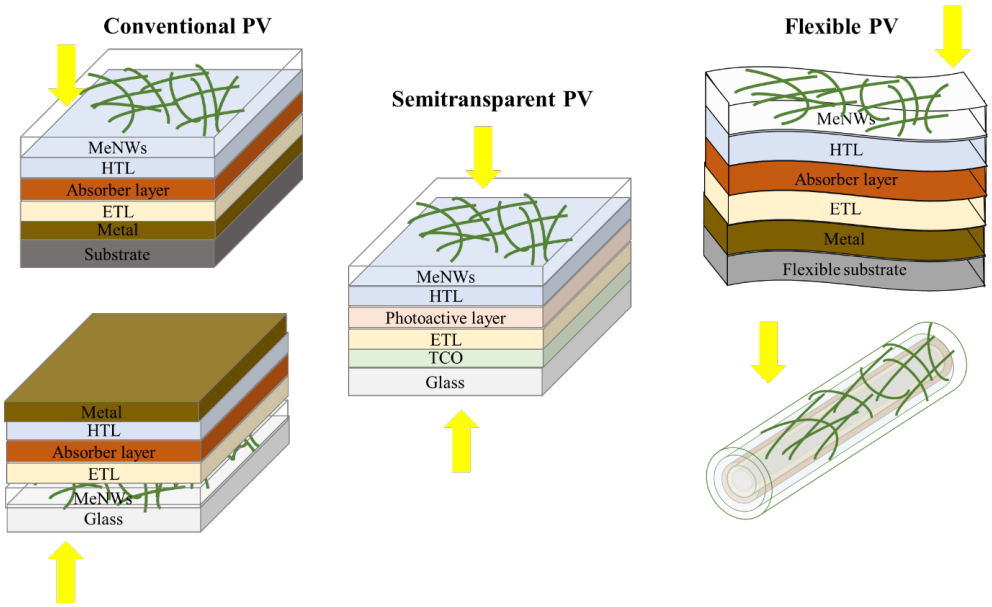

Figure 8. Schematic illustration of the representative solar cell architectures employing metal nanowire networks as the transparent electrode. They are conventional solar cells with a regular stacking architecture and inverted architecture, flexible solar cells with a planar architecture and fibre-shaped architecture and semitransparent solar cells.

Challenges and Future Directions

Despite the great progress made in the development of solution-processable high-throughput MNWNs for photovoltaics, there remain several challenges to overcome for practical and wide applications of MNWNs.

- Intrinsic limitations in the optical and electrical properties: MNWN transparent electrodes have a unique network geometry, where the conductive pathways come from the interconnected networks while the transparency is dependent on the voids [107]. For the electrical properties, the large contact resistance at the junctions of metal nanowires hampers its conductivity. Additionally, the voids between the junctions reduce the effective charge collection area in a solar cell. For the optical properties, the network geometry may increase the reflection loss [111]. Thermal annealing or chemical fusion will help reduce the junction resistance [112]. The "composite material strategy" will turn the non-conductive voids into effective charge pathways and minimize light loss, such as hybrid MNWNs with continuous transparent conductive thin films (ITO/MNWNs and PEDOT:PSS/ MNWNs)
- Thermal stability: Post-treatments are typically employed to further improve the electrical properties of MNWNs, such as thermal annealing. A fast annealing at 200 °C for 20 min can increase its conductivity by almost an order of magnitude, however, a dramatic degradation is seen at the temperature of >300 °C [147]. Optimizing the fabrication process of a solar cell may improve layer-to-layer compatibility and reduce the thermal budget of a complete device.
- Chemical stability: The large specific surface area of metal nanowires makes them more susceptible to oxygen and water in an ambient environment. A thin oxidation layer that gradually forms on the surface of the MNWNs will greatly increase the resistance. In addition, the reaction of metal nanowires with certain photoactive layers also poses a big issue in a device, such as perovskite solar cells. Whether MNWNs are used as the bottom electrode and in direct contact with the perovskite layer or used as the top electrode and separated from the perovskite layer, the halides will either immediately or eventually migrate to the surface of MNWNs to form unstable halide compounds [131]. Moreover, solvent compatibility needs to be considered when fabricating a solar cell. MNWNs are typically dispersed in polar solvents before

coating, such as water, ethanol and isopropyl alcohol, while perovskites are sensitive to water and ethanol [128,148,149]. To tackle the challenges discussed above, surface modification or passivation of MNWNs may help isolate metal nanowires from the reactive surroundings.

- Mechanical stability: Compared with vacuum-deposited films, MNWNs have a poorer adhesion to the substrates which inhibits their mechanical stability. Meanwhile, the junctions of the as-fabricated MNWNs are potential weak spots, especially under extreme deformations. Thermal welding or roll lamination may reinforce the adhesion of MNWNs to the substrate and metal nanowires to metal nanowires.

3.4. PEDOT:PSS

As the predominant candidate in conductive polymers, commercialization of PEDOT:PSS aqueous dispersion has been realized with the product name of Clevios for facile and scalable production of PEDOT:PSS films [150]. Various solution-based film depositions have been demonstrated in the fabrication of PEDOT:PSS films, such as doctor blading, screen printing, spin coating, ink-jet printing, etc. [22,151].

In photovoltaics, PEDOT:PSS has been extensively exploited either as a hole transport layer (a high work function of ∼4.9–5.2 eV) [152] or a transparent bottom/top electrode in polymer and perovskite solar cells [21]. In this section, we will focus on its role as a transparent conductor. Despite its high transparency, flexibility and stability, the conductivity of PEDOT:PSS is inferior to that of ITO and Ag nanowires. There are several strategies to improve the conductivity PEDOT:PSS: solvent treatment, doping and composite materials [153].

By introducing polar solvents such as dimethyl formamide (DMF) [154], dimethyl sulfoxide (DMSO) [155,156] and ethylene glycol (EG) [157] into the aqueous dispersion of PEDOT:PSS, its conductivity can be increased by up to one order of magnitude. In addition, post-treatment of the PEDOT:PSS film with strong acid such as H_2SO_4 [158,159], has also been demonstrated as an effective way to improve its conductivity to a comparable value as that of ITO. The enhanced conductivity from solvent treatment is attributed to the better-orientated PEDOT chains and increased crystallinity of the film [159].

It is shown by researchers that doping PEDOT:PSS with ammonia-based compounds (e.g., cetyltrimethylammonium bromide/CTAB [160,161]) and ammonium metatungstate hydrate/AMH [162] can increase its conductivity and adjust the valence band for a higher power conversion efficiency in perovskite solar cells. Others found that doping PEDOT:PSS with organic salts (e.g., sodium citrate [163]) and inorganic salts (e.g., sodium chloride [164] and rubidium chloride [165]) could also effectively tune the work function, conductivity and film morphology of PEDOT:PSS which favours a higher Voc and FF in perovskite solar cells.

To achieve the synergetic effect of two different materials, many trials have been conducted to develop PEDOT: PSS-based composite materials for improved optical and electrical properties. Examples include PEDOT:PSS/Ag nanowires [166,167] and PEDOT:PSS/reduced graphene oxide [168]. However, extra design is typically required when a hybrid with a secondary component as PEDOT:PSS dispersion is acidic and corrosive.

In spite of the great efforts made to improve the conductivity of PEDOT:PSS, there is still room and need to further boost its conductivity for a higher J_{SC} in solar cells. The main design principle is to enhance the interactions between conductive PEDOT chains while isolating or reducing the insulating PSS segments. In addition, the acidity of PEDOT:PSS dispersion may corrode the layer underneath. Finding a co-solvent to increase the pH of PEDOT:PSS aqueous solution without compromising its performance or introducing a protection/isolation layer in-between may help resolve the issue.

3.5. Carbon Based Transparent Conductors

3.5.1. Graphene

Of the two promising carbon-based transparent electrode materials for PSCs, graphene seems to show more promise compared to the progress made with carbon nanotubes. It

is smoother, more transparent on a broad wavelength region, and more conductive [38]. In general, graphene exhibits a plethora of promising properties including low-sheet resistance, outstanding electrical conductivity, high optical transmittance, good mechanical properties and thermal and chemical stability for PSCs [36,39,169,170]. For thin-film solar cells, graphene is typically synthesized via chemical vapour deposition (CVD) as the large area of thin-layer graphene films with fewer defects that can be produced [36,171,172]. It is then annealed at no higher than in a 10:1 Ar:H_2 mixture for a monolayer of graphene [173].

PSCs with high performances usually have an n-i-p architecture consisting of a scaffold metal oxide such as TiO_2/perovskite material/hole transport material; however, PSCs with a reversed architecture or ones that adopt an n-i-p structure have attracted a lot of interest because of their low processing temperature, which can lead to lowering manufacturing costs and facile manufacturing processes on different substrates and for other device layers such as multi-junction solar cells [170,174]. For the electrodes, graphene is typically used to replace the top electrode or anode. There is generally a lot less effort and progress put into replacing metallic cathodes in PVs; however, it would be advantageous to do so to increase the flexibility and the overall transparency of the device specifically for FPSCs [175]. In a standard layer-by-layer design, graphene is the very top layer sealed with a layer of poly(3,4 thlene-dioxythiophene: poly(styrenesulfonate) (PEDOT:PSS) and/or D-sorbital [170]. These are used as adhesion layers in the lamination process of layering graphene, but also between graphene and the perovskite material within the solar cell stack [36]. Below the perovskite material is the bottom electrode or cathode, usually made of fluorine-doped tin oxide (FTO), ITO, Au or Al [25]. The bottom-most layer is the substrate for rigid and flexible PSCs (i.e., glass, polyethylene naphthalate (PEN), polyethylene terephthalate (PET)).

To improve the electrical and optical properties of graphene-based transparent electrodes, multiple studies performed a combination of both stacking multiple monolayers of graphene, sealing PEDOT:PSS and D-sorbital, and doping it with molybdenum trioxide (MoO_3), hydrochloric acid (HCl), nitric acid (HNO_3), gold (III) and chloride ($AuCl_3$). Multiple studies have shown a trade-off between stacking thin graphene layers to get a lower sheet resistance and the amount of transmittance. Multilayer graphene films, individually produced via CVD, are fabricated using a layer-by-layer (LBL) transfer method. A study by You et al. revealed that two-layer graphene produces the highest PCE when comparing multilayer-graphene electrodes. Another study by Li et al. that doped graphene HNO_3 and stacked up to four layers showed that the addition of each layer decreases the transmittance by about 2.3%. Overall, stacking more layers of graphene has resulted in less transmittance. Multilayer graphene helps accommodate an improved electrical conductivity; however, an excess of graphene nanosheets would fold together, which leads to a significant decrease of transmittance of up to 80% [36,39,176].

In addition, graphene can also be doped, specifically, *p*-doping to increase the PCE. This enhances the conductivity by increasing the carrier concentration and allows for the desired energy level to become aligned with the highest occupied molecular orbital (HOMO) level of the hole transporting layer (HTL) [35,170]. More specifically, the hydrophilicity of graphene is improved by evaporating a layer of MoO_3. The presence of hydroxyl groups on MoO_3 allows the spreading of PEDOT:PSS to create an interfacial layer that decreases the large energy difference between graphene and HOMO of active layer poly(3-hexythiophene-2, 5-diyl):[6,6]-phenyl C61 butyric acid methyl ester (P3HT:PCBM) [170,177]. Since a monolayer of graphene suffers from low conductivity, this can be overcome by doping or mixing other elements into the graphene matrix.

3.5.2. Carbon Nanotubes

In addition to graphene-based electrodes, another viable carbon-based material for transparent electrodes in solar cells is the use of carbon nanotubes. Carbon nanotubes can be broken into the three following categories: single-walled (SWNTs), double-walled (DWNTs), and multi-walled (MWNTs) carbon nanotubes. CNTs are single layers of graphene bent into cylinders. SWNTs contain a single cylinder of graphene, whereas DWNTs and MWNTs

contain two or more concentric cylinders of graphene, respectively. Thus, the approaches to prepare and optimize carbon nanotubes differ drastically from that of graphene due to their distinguished geometries (e.g., 1D, 2D) and properties [38].

Like graphene, CNTS also have high optical transmittance and electrical conductivity which is what makes them attractive for transparent electrodes and hole collectors. In PSC electrodes, they are electron acceptors or hole collectors in junction with active n-type layer, specifically PEDOT:PSS layer [33]. These two properties of CNTs are critical parameters in the utility of the application of transparent electrodes. In addition, they are known for their ease of fabrication and good mechanical durability. Their stability is due to their hydrophobic nature [38]. This prevents moisture invasion in devices; however, it also poses a challenge for uniform film fabrication due to the Vander Waals interaction [38,178].

In general, most CNTs are fabricated using the floating catalyst CVD method due to the relatively low production cost, high efficiency and scalable nature [178,179]. This method is based on ferrocene vapour decomposition in a CO_2 atmosphere [38,180]. More specifically, Jeon et al. created a simpler solution for fabricated processible DWNTs, which were grown by a catalytic high temperature chemical vapour deposition [181]. Overall, longer, conductive and less defective and pure CNTs are desired for transparent CNT films to gain continued widespread various commercial applications [182]. The primary method to improve the conductive performance of CNTs in PSCs and FPSCs is to dope or introduce electron donors that intercalate [183]. CNTs have been doped with MoO_3, HNO_3, trifluoromethanesulfonic acid (TFMS), bromine (Br_2), thionyl chloride ($SOCl_2$), nafion and tetrafluorotetracyano–quinodimethane ($TCNQF_4$) [184–188].

Moreover, doping DWNTs specifically with TFMS increased the PCE from 14.4% to 16.0% in an inverted planar PSC with specified solar architecture, as listed in Table 3. This improvement can also be noted in the fill factor (FF) and the open circuit voltage (V_{OC}) which can be attributed to better energy alignment between DWNT and PTAA after doping. In terms of durability, TFMS doping had a lasting effect of more than 100 days, whereas the HNO_3 doping effect disappeared after 10 days [189]. According to Xu et al., HNO_3 is an effective dopant; however, there is also an energy level mismatch between HNO_3-doped CNTs and the perovskite layer. This could also be due to the damage that HNO_3 does to the structure of SWNTs and possibly DWNTs [38].

Other studies have added a bilayer of MoO_3 to the PSC device with variations in thickness. Unlike doping CNTs with TFMS or HNO_3, multiple studies show that PSCs with MoO_3-doped CNTs electrodes have much lower PCEs [180]. This is due to the energy level mismatch between PEDOT:PSS and MoO_3. Ultrathin layers of MoO_3 with 2 and 6 nm thicknesses were deposited via vacuum thermal evaporator which was followed by anaerobic annealing at 115 °C for 30 min. Thicker layers led to a larger energy misalignment with a lower transmission. This can be noted again in Table 3, where the thickness of the MoO_3 bilayer increased (2 nm to 6 nm) and the PCE decreased from 12.8% to 11.0%. Despite its PCE performance relative to other dopants, MoO_3 is one of the most established and chemically stable dopants for both CNTs and graphene.

The current main challenges with CNTs are balancing out the wettability and conductivity. Oftentimes, many of the chemical treatments to increase the hydrophilicity decrease the conductivity because it introduces many oxygen-containing groups [190]. Thus, there is a need for improving current wettability techniques for CNTs. Additionally, it is also difficult to optimize between transmission and conductivity. As the CNT–film thickness increases, the conductivity increases since percolation begins at around 50 nm thick. However, the thickness of a CNT–electrode layer that yields a high transmission range of 90–95% is 5–10 nm. This is because of the low percolation threshold of CNTs, which is due to the one-dimensional nature of the tubes and bundles.

Table 3. Literature summary of carbon-material based transparent electrodes used in solar cells.

Device Architecture	FF (%)	PCE (%)	T (%)
Glass/AgNWs-G1/SnO_2/Perovskite/Carbon [39]	43.64	10.2	88
Glass/AgNWs-G2/SnO_2/Perovskite/Carbon [39]	66.46	15.31	86
Glass/G-2(HNO_3-doped)/PEDOT:PSS/n-Si/LiF/Al [36]	40	5.35	97
Glass/G-3(HNO_3-doped)/PEDOT:PSS/n-Si/LiF/Al [36]	39	5.48	95
Glass/G-4(HNO_3-doped)/PEDOT:PSS/n-Si/LiF/Al [36]	47	5.76	93
Glass/G-3(undoped)/PEDOT:PSS/n-Si/LiF/Al [36]	36	3.92	90
Glass/G-3(undoped)-(1 month)/PEDOT:PSS/n-Si/LiF/Al [36]	38	4.84	na
Glass/FTO/Compact-TiO_2/$MAPbI_{3-x}Cl_x$/Spiro-OMeTAD/PEDOT:PSS/G-1 [169,176]	59.07	8.74	93
Glass/FTO/Compact-TiO_2/$MAPbI_{3-x}Cl_x$/Spiro-OMeTAD/PEDOT:PSS/G-2 [169,176]	71.72	12.03	88
Glass/FTO/Compact-TiO_2/$MAPbI_{3-x}Cl_x$/Spiro-OMeTAD/PEDOT:PSS/G-3 [169,176]	67.58	10.94	83
Glass/FTO/Compact-TiO_2/$MAPbI_{3-x}Cl_x$/Spiro-OMeTAD/PEDOT:PSS/G-4 [176]	68.37	10.18	na
Glass/Graphene/MoO_3-1 nm/PEDOT:PSS/Perovskite/C60/BCP/LiF/Al [170]	45	6.7	89
Glass/Graphene/MoO_3-2 nm/PEDOT:PSS/Perovskite/C60/BCP/LiF/Al [170]	72	16.1	na
Glass/Graphene/MoO_3-4 nm/PEDOT:PSS/Perovskite/C60/BCP/LiF/Al [170]	70	15.9	na
G-3/MoO_3+PEDOT:PSS/P3HT:PCBM/LiF/Al (HCl interlayer and HNO_3 doping) [191]	45	1.9	na
Graphene/PEDOT:PSS/P3HT:PCBM/LiF/Al [191]	51	2.5	na
Glass/SnO_2:F/TiO_2/$CH_3NH_3PbI_3$/spiro-OMeTAD/graphene [192]	56.6	8.4	64
PET/APTES/$AuCl_3$-G/PEDOT:PSS/$FAPbI_{3-x}Br_x$/PCBM/Al [193]	76.2	17.4	na
PET/APTES/$AuCl_3$-G/PEDOT:PSS/$MAPbI_3$/PCBM/Al [193]	75.7	15.6	na
PET/AuCl3-G/PEDOT:PSS/$MaPbI_3$ [193]	75.8	15.5	na
DWNT/PTAA/$MA_{0.6}FA_{0.4}PbI_{2.9}Br_{0.1}$/BCP/Cu [189]	69.1	14.4	na
HNO_3-doped DWNT/PTAA/$MA_{0.6}FA_{0.4}PbI_{2.9}Br_{0.1}$/BCP/Cu [189]	71.7	15.6	na
TFMS-doped DWNT/PTAA/$MA_{0.6}FA_{0.4}PbI_{2.9}Br_{0.1}$/BCP/Cu [189]	75	16	na
Glass/SWNT/IPA-PEDOT:PSS/$CH_3NH_3PBI_3$/PC61BM/Al [194]	50	4.01	na
Glass/SWNT/surfactant-PEDOT:PSS/$CH_3NH_3PBI_3$/PC61BM/Al [194]	38	1.85	na
Glass/70 v/v% HNO_3-SWNT/PEDOT:PSS/$CH_3NH_3PBI_3$/PC61BM/Al [194]	55	5.96	na
Glass/50 v/v% HNO_3-SWNT/PEDOT:PSS/$CH_3NH_3PBI_3$/PC61BM/Al [194]	52	5.82	na
Glass/35 v/v% HNO_3-SWNT/PEDOT:PSS/$CH_3NH_3PBI_3$/PC61BM/Al [194]	54	5.7	na
Glass/15 v/v% HNO_3-SWNT/PEDOT:PSS/$CH_3NH_3PBI_3$/PC61BM/Al [194]	39	3.80	na
Glass/SWNT/MoO_3/$CH_3NH_3PBI_3$/PC61BM/Al [194]	28	0.05	na
Glass/SWNT/MoO_x/PEDOT:PSS/$CH_3NH_3PBI_3$/PC61BM/Al [194]	42	2.09	na
FTO/TiO_2/$(FAPbI_3)_{1-x}(MAPbBr_3)_x$/SWNT:Spiro-OMeTAD/Au [195]	61	15.5	na
FTO/TiO_2/$(FAPbI_3)_{1-x}(MAPbBr_3)_x$/SWNT/Au [195]	46	11	na
Ti-125(μm)Foil/TiO_2 NTs + $CH_3NH_3PBI_3$/CNT+spiro-OMeTAD [178]	62	3.90	na
Ti-25(μm)Foil/TiO_2 NTs + $CH_3NH_3PBI_3$/CNT+spiro-OMeTAD [178]	63	4.83	na
Glass/SWNT/PEDOT:PSS/P3HT:PCBM/Al [33]	29	1.5	na
Glass/SWNT/P3HT:PCBM/Al [33]	29.8	0.5	na
Glass/SWNT/MoO_3-2 nm/PEDOT:PSS/$MAPbI_3$/C60/BCP/LiF/Al [180]	76	12.8	na
Glass/SWNT/MoO_3-6 nm/PEDOT:PSS/$MAPbI_3$/C60/BCP/LiF/Al [180]	71	11	na
Glass/SWNT-HNO_3/PEDOT:PSS/$MAPbI_3$/C60/BCP/LiF/Al [180]	78	15.3	na
PEN/SWNT/MoO_3-2 nm/PEDOT:PSS/$MAPbI_3$/C60/BCP/LiF/Al [180]	65	11	na

Graphene (G), One Layer of Graphene (G-1); Two Layers of Graphene (G-2); Three Layers of Graphene (G-3); Four of Layers of Graphene (G-4); Silver Nanowires (AgNWs); Poly(3-hexylthiophene):phenyl-C60-butyric acid methyl ester (P3HT:PCBM); Poly(3,4 thlene-dioxythiophene: poly(styrenesulfonate) (PEDOT:PSS); Nitric Acid (HNO_3); Gold (III) Chloride ($AuCl_3$); 2,2′,7,7′,tetrakis(N, N-di-p-methoxyphenylamine)-9, 9-spirobifluorene (Spiro-OMeTAD); Polyethylene Terephthalate (PET); Bathocuproine (BCP); Molybdenum Trioxide (MoO_3); Single-Walled Carbon Nanotubes (SWNT); Double-Walled Carbon Nanotubes (DWNT); 3-aminopropyltriethoxysilane (APTES); Lithium Fluoride (LiF); TiO_2 NTs (Titanium Dioxide); Isopropanol (IPA); Trifluoromethanesulfonic Acid (TFMS); Poly(triaryl amine) (PTA).

4. Conclusions

Most of the dominating photovoltaic technology presently uses crystalline Si and various perovskite compounds as absorbers with TCMs in the back and front sides along with metal contacts. These TCMs act as a membrane that blocks one carrier and selects the other, thereby defining the current flow direction and making the solar cell work. Various *n*-and *p*-type TCMs have been extensively used in solar cells. However, low conductivity, mobility and high contact resistance limit the performance of solar cell devices. To overcome this issue, a lot of research has been going on in developing high-performing TCMs.

Despite the great progress made in the development of solution-processable high throughput MNWNs for photovoltaics, there remain several challenges pertaining to optoelectronic properties, thermal stability, chemical stability and mechanical stability. Several pathways such as thermal annealing, chemical fusion and composite material

strategy have been proposed to improve optoelectronic properties of MNWNs. Further, the thermal, chemical and mechanical stability can be improved via optimizing the fabrication process, surface modification, surface passivation and thermal welding/roll lamination. In the case of polymer-based TCMs such as PEDOT:PSS, conductivity still remains very low. However, finding a suitable co-solvent to increase the pH of PEDOT:PSS aqueous solution may enhance overall optoelectronic performance.

PCE of PSCs resulted in increased efficiencies with the integration of transparent graphene and CNTs electrodes via optimizing between conductivity and transparency. Additionally, the mechanical transferring of monolayer graphene still remains a major challenge. Further, the current main challenges with CNTs are balancing out the wettability and conductivity. Oftentimes, many of the chemical treatments to increase hydrophilicity decrease the conductivity because it introduces many oxygen-containing groups. Thus, there is a need for improving current wettability techniques for CNTs.

Author Contributions: Conceptualization, X.X. and S.K.M.; writing, S.K.M., X.X., H.R.G. and G.G.; review and editing, S.K.M., X.X., H.R.G. and G.G. All authors have read and agreed to the published version of the manuscript.

Funding: This research was funded by U.S. Department of Energy by Lawrence Livermore National Laboratory under Contract No. DE-AC52-07NA27344.

Institutional Review Board Statement: Not applicable.

Informed Consent Statement: Not applicable.

Data Availability Statement: Not applicable.

Conflicts of Interest: The authors declare no conflict of interest.

Abbreviations

The following abbreviations are used in this manuscript:

TCM	Transparent conducting material
TC	Transparent conductor
LED	Light-emitting diode
CBM	Conduction band minima
VBM	Valence band maxima
ALD	Atomic layer deposition
CBD	Chemical bath deposition
PLD	Pulsed laser deposition
ITO	Tin-doped indium oxide
AZO	Al-doped zinc oxide
IZO	Indium zinc oxide
FTO	Fluorine-doped tin oxide
UTMF	Ultra-thin metal film
PEC	Power conversion efficiency
FPSC	Flexible perovskite solar cell
SWCNT	Single-walled carbon nanotube
MNWN	Metal nanowire network

References

1. Fuchs, K. The conductivity of thin metallic films according to the electron theory of metals. In *Mathematical Proceedings of the Cambridge Philosophical Society*; Cambridge University Press: Cambridge, UK, 1938; Volume 34, pp. 100–108.
2. Mayadas, A.; Shatzkes, M. Electrical-resistivity model for polycrystalline films: The case of arbitrary reflection at external surfaces. *Phys. Rev. B* **1970**, *1*, 1382. [CrossRef]
3. Ginley, D.S.; Bright, C. Transparent conducting oxides. *MRS Bull.* **2000**, *25*, 15–18. [CrossRef]
4. Gordon, R.G. Criteria for choosing transparent conductors. *MRS Bull.* **2000**, *25*, 52–57. [CrossRef]
5. Ginley, D.S.; Hosono, H.; Paine, D.C. *Handbook of Transparent Conductors*; Springer Science & Business Media: New York, NY, USA, 2010.

6. Klein, A.; Körber, C.; Wachau, A.; Säuberlich, F.; Gassenbauer, Y.; Harvey, S.P.; Proffit, D.E.; Mason, T.O. Transparent conducting oxides for photovoltaics: Manipulation of fermi level, work function and energy band alignment. *Materials* **2010**, *3*, 4892–4914. [CrossRef]
7. Oh, B.Y.; Jeong, M.C.; Moon, T.H.; Lee, W.; Myoung, J.M.; Hwang, J.Y.; Seo, D.S. Transparent conductive Al-doped ZnO films for liquid crystal displays. *J. Appl. Phys.* **2006**, *99*, 124505. [CrossRef]
8. Grilli, M.L.; Sytchkova, A.; Boycheva, S.; Piegari, A. Transparent and conductive Al-doped ZnO films for solar cells applications. *Phys. Status Solidi* **2013**, *210*, 748–754. [CrossRef]
9. Hagendorfer, H.; Lienau, K.; Nishiwaki, S.; Fella, C.M.; Kranz, L.; Uhl, A.R.; Jaeger, D.; Luo, L.; Gretener, C.; Buecheler, S.; et al. Highly transparent and conductive ZnO: Al thin films from a low temperature aqueous solution approach. *Adv. Mater.* **2014**, *26*, 632–636. [CrossRef]
10. Ellmer, K. Past achievements and future challenges in the development of optically transparent electrodes. *Nat. Photonics* **2012**, *6*, 809–817. [CrossRef]
11. Fortunato, E.; Ginley, D.; Hosono, H.; Paine, D.C. Transparent conducting oxides for photovoltaics. *MRS Bull.* **2007**, *32*, 242–247. [CrossRef]
12. Delahoy, A.E.; Guo, S. *Transparent Conducting Oxides for Photovoltaics*; Wiley Online Library: Hoboken, NJ, USA, 2011; pp. 716–796.
13. Morales-Masis, M.; De Wolf, S.; Woods-Robinson, R.; Ager, J.W.; Ballif, C. Transparent electrodes for efficient optoelectronics. *Adv. Electron. Mater.* **2017**, *3*, 1600529. [CrossRef]
14. Granqvist, C.G. Transparent conductors as solar energy materials: A panoramic review. *Sol. Energy Mater. Sol. Cells* **2007**, *91*, 1529–1598.
15. Guo, C.F.; Ren, Z. Flexible transparent conductors based on metal nanowire networks. *Mater. Today* **2015**, *18*, 143–154. [CrossRef]
16. Sannicolo, T.; Lagrange, M.; Cabos, A.; Celle, C.; Simonato, J.P.; Bellet, D. Metallic nanowire-based transparent electrodes for next generation flexible devices: A review. *Small* **2016**, *12*, 6052–6075. [CrossRef]
17. Liu, J.; Jia, D.; Gardner, J.M.; Johansson, E.M.; Zhang, X. Metal nanowire networks: Recent advances and challenges for new generation photovoltaics. *Mater. Today Energy* **2019**, *13*, 152–185. [CrossRef]
18. Xia, Y.; Dai, S. Review on applications of PEDOTs and PEDOT:PSS in perovskite solar cells. *J. Mater. Sci. Mater. Electron.* **2021**, *32*, 12746–12757. [CrossRef]
19. Palumbiny, C.M.; Heller, C.; Schaffer, C.J.; Körstgens, V.; Santoro, G.; Roth, S.V.; Müller-Buschbaum, P. Molecular reorientation and structural changes in cosolvent–treated highly conductive PEDOT:PSS electrodes for flexible indium tin oxide-free organic electronics. *J. Phys. Chem. C* **2014**, *118*, 13598–13606. [CrossRef]
20. Reza, K.M.; Mabrouk, S.; Qiao, Q. A review on tailoring PEDOT:PSS layer for improved performance of perovskite solar cells. *Proc. Nat. Res. Soc.* **2018**, *2*, 02004. [CrossRef]
21. Han, W.; Ren, G.; Liu, J.; Li, Z.; Bao, H.; Liu, C.; Guo, W. Recent progress of inverted perovskite solar cells with a modified PEDOT:PSS hole transport layer. *ACS Appl. Mater. Interfaces* **2020**, *12*, 49297–49322. [CrossRef]
22. Hu, L.; Song, J.; Yin, X.; Su, Z.; Li, Z. Research progress on polymer solar cells based on PEDOT:PSS electrodes. *Polymers* **2020**, *12*, 145. [CrossRef]
23. Park, H.H. Transparent electrode techniques for semitransparent and tandem perovskite solar cells. *Electron. Mater. Lett.* **2021**, *17*, 18–32. [CrossRef]
24. Cai, M.; Wu, Y.; Chen, H.; Yang, X.; Qiang, Y.; Han, L. Cost-performance analysis of perovskite solar modules. *Adv. Sci.* **2017**, *4*, 1600269. [CrossRef]
25. Que, M.; Zhang, B.; Chen, J.; Yin, X.; Yun, S. Carbon-based electrodes for perovskite solar cells. *Mater. Adv.* **2021**, *2*, 5560–5579. [CrossRef]
26. Tonui, P.; Oseni, S.O.; Sharma, G.; Yan, Q.; Mola, G.T. Perovskites photovoltaic solar cells: An overview of current status. *Renew. Sustain. Energy Rev.* **2018**, *91*, 1025–1044. [CrossRef]
27. Bisquert, J.; Juarez-Perez, E.J. The causes of degradation of perovskite solar cells. *J. Phys. Chem. Lett.* **2019**, *10*, 5889–5891. [CrossRef]
28. Miyata, A.; Mitioglu, A.; Plochocka, P.; Portugall, O.; Wang, J.T.W.; Stranks, S.D.; Snaith, H.J.; Nicholas, R.J. Direct measurement of the exciton binding energy and effective masses for charge carriers in organic–inorganic tri-halide perovskites. *Nat. Phys.* **2015**, *11*, 582–587. [CrossRef]
29. Liu, M.; Johnston, M.B.; Snaith, H.J. Efficient planar heterojunction perovskite solar cells by vapour deposition. *Nature* **2013**, *501*, 395–398. [CrossRef]
30. Hadadian, M.; Smått, J.H.; Correa-Baena, J.P. The role of carbon-based materials in enhancing the stability of perovskite solar cells. *Energy Environ. Sci.* **2020**, *13*, 1377–1407. [CrossRef]
31. Dunlap-Shohl, W.A.; Zhou, Y.; Padture, N.P.; Mitzi, D.B. Synthetic approaches for halide perovskite thin films. *Chem. Rev.* **2018**, *119*, 3193–3295. [CrossRef] [PubMed]
32. Guo, M.; Wei, C.; Liu, C.; Zhang, K.; Su, H.; Xie, K.; Zhai, P.; Zhang, J.; Liu, L. Composite electrode based on single-atom Ni doped graphene for planar carbon-based perovskite solar cells. *Mater. Des.* **2021**, *209*, 109972. [CrossRef]
33. Van De Lagemaat, J.; Barnes, T.M.; Rumbles, G.; Shaheen, S.E.; Coutts, T.J.; Weeks, C.; Levitsky, I.; Peltola, J.; Glatkowski, P. Organic solar cells with carbon nanotubes replacing In_2O_3: Sn as the transparent electrode. *Appl. Phys. Lett.* **2006**, *88*, 233503. [CrossRef]

34. Christians, J.A.; Pierre, A.; Miranda, H.; Kamat, P.V. Transformation of the excited state and photovoltaic efficiency of $CH_3NH_3PbI_3$ perovskite upon controlled exposure to humidified air. *J. Am. Chem. Soc.* **2015**, *137*, 1530–1538. [CrossRef] [PubMed]
35. Lee, K.T.; Park, D.H.; Baac, H.W.; Han, S. Graphene-and carbon-nanotube-based transparent electrodes for semitransparent solar cells. *Materials* **2018**, *11*, 1503. [CrossRef] [PubMed]
36. Li, P.; Chen, C.; Zhang, J.; Li, S.; Sun, B.; Bao, Q. Graphene-based transparent electrodes for hybrid solar cells. *Front. Mater.* **2014**, *1*, 26. [CrossRef]
37. Liang, L.; Cai, Y.; Li, X.; Nazeeruddin, M.K.; Gao, P. All that glitters is not gold: Recent progress of alternative counter electrodes for perovskite solar cells. *Nano Energy* **2018**, *52*, 211–238. [CrossRef]
38. Xu, Y.; Lin, Z.; Wei, W.; Hao, Y.; Liu, S.; Ouyang, J.; Chang, J. Recent Progress of Electrode Materials for Flexible Perovskite Solar Cells. *Nano-Micro Lett.* **2022**, *14*, 1–30. [CrossRef]
39. Zhou, J.; Li, S.; Lv, X.; Li, X.; Li, Y.; Zheng, Y.Z.; Tao, X. Ultra-low-cost all-air processed carbon-based perovskite solar cells from bottom electrode to counter electrode. *J. Power Sources* **2020**, *478*, 228764. [CrossRef]
40. Langmuir, I. Oscillations in ionized gases. *Proc. Natl. Acad. Sci. USA* **1928**, *14*, 627–637. [CrossRef]
41. Wang, Y.; Plummer, E.; Kempa, K. Foundations of plasmonics. *Adv. Phys.* **2011**, *60*, 799–898. [CrossRef]
42. Gao, J.; Kempa, K.; Giersig, M.; Akinoglu, E.M.; Han, B.; Li, R. Physics of transparent conductors. *Adv. Phys.* **2016**, *65*, 553–617. [CrossRef]
43. Drude, P. Zur elektronentheorie der metalle. *Ann. Phys.* **1900**, *306*, 566–613. [CrossRef]
44. Coutts, T.J.; Young, D.L.; Li, X. Characterization of transparent conducting oxides. *MRS Bull.* **2000**, *25*, 58–65. [CrossRef]
45. Ginley, D.; Coutts, T.; Perkins, J.; Young, D.; Li, X.; Parilla, P. Next-generation transparent conducting oxides for photovoltaic cells: An overview. In *MRS Online Proceedings Library (OPL)*; Cambridge University Press: Cambridge, UK, 2001; Volume 668.
46. Holland, L.; Siddall, G. The properties of some reactively sputtered metal oxide films. *Vacuum* **1953**, *3*, 375–391. [CrossRef]
47. Hamberg, I.; Granqvist, C.G. Evaporated Sn-doped In_2O_3 films: Basic optical properties and applications to energy-efficient windows. *J. Appl. Phys.* **1986**, *60*, R123–R160. [CrossRef]
48. Haacke, G. Transparent electrode properties of cadmium stannate. *Appl. Phys. Lett.* **1976**, *28*, 622–623. [CrossRef]
49. Haacke, G. Evaluation of cadmium stannate films for solar heat collectors. *Appl. Phys. Lett.* **1977**, *30*, 380–381. [CrossRef]
50. Miyata, N.; Miyake, K.; Nao, S. Physical properties of cadmium-tin oxide films deposited by dc reactive sputtering. *Thin Solid Film.* **1979**, *58*, 385–389. [CrossRef]
51. Minami, T.; Sato, H.; Nanto, H.; Takata, S. Group III impurity doped zinc oxide thin films prepared by RF magnetron sputtering. *Jpn. J. Appl. Phys.* **1985**, *24*, L781. [CrossRef]
52. Minami, T.; Sonohara, H.; Kakumu, T.; Takata, S.T.S. Highly transparent and conductive $Zn_2In_2O_5$ thin films prepared by RF magnetron sputtering. *Jpn. J. Appl. Phys.* **1995**, *34*, L971. [CrossRef]
53. Kasar, R.; Deshpande, N.; Gudage, Y.; Vyas, J.; Sharma, R. Studies and correlation among the structural, optical and electrical parameters of spray-deposited tin oxide (SnO_2) thin films with different substrate temperatures. *Phys. B Condens. Matter* **2008**, *403*, 3724–3729. [CrossRef]
54. Muthukumar, A.; Giusti, G.; Jouvert, M.; Consonni, V.; Bellet, D. Fluorine-doped SnO_2 thin films deposited on polymer substrate for flexible transparent electrodes. *Thin Solid Film.* **2013**, *545*, 302–309. [CrossRef]
55. Powell, M.J.; Williamson, B.A.; Baek, S.Y.; Manzi, J.; Potter, D.B.; Scanlon, D.O.; Carmalt, C.J. Phosphorus doped SnO_2 thin films for transparent conducting oxide applications: Synthesis, optoelectronic properties and computational models. *Chem. Sci.* **2018**, *9*, 7968–7980. [CrossRef] [PubMed]
56. Lekshmy, S.S.; Daniel, G.P.; Joy, K. Microstructure and physical properties of sol gel derived SnO_2:Sb thin films for optoelectronic applications. *Appl. Surf. Sci.* **2013**, *274*, 95–100. [CrossRef]
57. Fukumoto, M.; Nakao, S.; Shigematsu, K.; Ogawa, D.; Morikawa, K.; Hirose, Y.; Hasegawa, T. High mobility approaching the intrinsic limit in Ta-doped SnO_2 films epitaxially grown on TiO_2 (001) substrates. *Sci. Rep.* **2020**, *10*, 1–9. [CrossRef] [PubMed]
58. Prakash, A.; Xu, P.; Faghaninia, A.; Shukla, S.; Ager, J.W.; Lo, C.S.; Jalan, B. Wide bandgap $BaSnO_3$ films with room temperature conductivity exceeding 104 S cm^{-1}. *Nat. Commun.* **2017**, *8*, 1–9. [CrossRef] [PubMed]
59. Ueda, N.; Hosono, H.; Waseda, R.; Kawazoe, H. Synthesis and control of conductivity of ultraviolet transmitting β-Ga_2O_3 single crystals. *Appl. Phys. Lett.* **1997**, *70*, 3561–3563. [CrossRef]
60. Kumar, A.; Maurya, S.; Chawla, S.; Patwardhan, S.; Kavaipatti, B. Effect of thickness on metal to semiconductor transition in La doped $BaSnO_3$ films deposited on high mismatch LSAT substrates. *Appl. Phys. Lett.* **2019**, *114*, 212103. [CrossRef]
61. Schlom, D.G.; Pfeiffer, L.N. Upward mobility rocks! *Nat. Mater.* **2010**, *9*, 881–883. [CrossRef]
62. Raghavan, S.; Schumann, T.; Kim, H.; Zhang, J.Y.; Cain, T.A.; Stemmer, S. High-mobility $BaSnO_3$ grown by oxide molecular beam epitaxy. *Apl Mater.* **2016**, *4*, 016106. [CrossRef]
63. Banerjee, A.; Chattopadhyay, K. Recent developments in the emerging field of crystalline p-type transparent conducting oxide thin films. *Prog. Cryst. Growth Charact. Mater.* **2005**, *50*, 52–105. [CrossRef]
64. Kawazoe, H.; Yanagi, H.; Ueda, K.; Hosono, H. Transparent p-type conducting oxides: Design and fabrication of p-n heterojunctions. *MRS Bull.* **2000**, *25*, 28–36. [CrossRef]
65. Hautier, G.; Miglio, A.; Ceder, G.; Rignanese, G.M.; Gonze, X. Identification and design principles of low hole effective mass p-type transparent conducting oxides. *Nat. Commun.* **2013**, *4*, 2292. [CrossRef] [PubMed]

66. Kawazoe, H.; Yasukawa, M.; Hyodo, H.; Kurita, M.; Yanagi, H.; Hosono, H. P-type electrical conduction in transparent thin films of $CuAlO_2$. *Nature* **1997**, *389*, 939–942. [CrossRef]
67. Duan, N.; Sleight, A.; Jayaraj, M.; Tate, J. Transparent p-type conducting $CuScO_{2+x}$ films. *Appl. Phys. Lett.* **2000**, *77*, 1325–1326. [CrossRef]
68. Ingram, B.J.; Harder, B.J.; Hrabe, N.W.; Mason, T.O.; Poeppelmeier, K.R. Transport and defect mechanisms in cuprous delafossites: $CuScO_2$ and $CuYO_2$. *Chem. Mater.* **2004**, *16*, 5623–5629. [CrossRef]
69. Nagarajan, R.; Draeseke, A.; Sleight, A.; Tate, J. p-type conductivity in $CuCr_{1-x}Mg_xO_2$ films and powders. *J. Appl. Phys.* **2001**, *89*, 8022–8025. [CrossRef]
70. Nagarajan, R.; Duan, N.; Jayaraj, M.; Li, J.; Vanaja, K.; Yokochi, A.; Draeseke, A.; Tate, J.; Sleight, A. p-Type conductivity in the delafossite structure. *Int. J. Inorg. Mater.* **2001**, *3*, 265–270. [CrossRef]
71. Jayaraj, M.; Draeseke, A.; Tate, J.; Sleight, A. p-Type transparent thin films of CuY1- xCaxO2. *Thin Solid Film.* **2001**, *397*, 244–248. [CrossRef]
72. Ueda, K.; Inoue, S.; Hirose, S.; Kawazoe, H.; Hosono, H. Transparent p-type semiconductor: LaCuOS layered oxysulfide. *Appl. Phys. Lett.* **2000**, *77*, 2701–2703. [CrossRef]
73. Hiramatsu, H.; Kamiya, T.; Tohei, T.; Ikenaga, E.; Mizoguchi, T.; Ikuhara, Y.; Kobayashi, K.; Hosono, H. Origins of hole doping and relevant optoelectronic properties of wide gap p-type semiconductor, LaCuOSe. *J. Am. Chem. Soc.* **2010**, *132*, 15060–15067. [CrossRef]
74. Tanaka, T.; Kawabata, K.; Hirose, M. Transparent, conductive CuI films prepared by rf-dc coupled magnetron sputtering. *Thin Solid Film.* **1996**, *281*, 179–181. [CrossRef]
75. Sirimanne, P.; Rusop, M.; Shirata, T.; Soga, T.; Jimbo, T. Characterization of transparent conducting CuI thin films prepared by pulse laser deposition technique. *Chem. Phys. Lett.* **2002**, *366*, 485–489. [CrossRef]
76. Grundmann, M.; Schein, F.L.; Lorenz, M.; Böntgen, T.; Lenzner, J.; von Wenckstern, H. Cuprous iodidea p-type transparent semiconductor: History and novel applications. *Phys. Status Solidi* **2013**, *210*, 1671–1703. [CrossRef]
77. Diamond, A.M.; Corbellini, L.; Balasubramaniam, K.; Chen, S.; Wang, S.; Matthews, T.S.; Wang, L.W.; Ramesh, R.; Ager, J.W. Copper-alloyed ZnS as a p-type transparent conducting material. *Phys. Status Solidi* **2012**, *209*, 2101–2107. [CrossRef]
78. Xu, X.; Bullock, J.; Schelhas, L.T.; Stutz, E.Z.; Fonseca, J.J.; Hettick, M.; Pool, V.L.; Tai, K.F.; Toney, M.F.; Fang, X.; et al. Chemical Bath Deposition of p-Type Transparent, Highly Conducting $(CuS)_x$:$(ZnS)_{1-x}$ Nanocomposite Thin Films and Fabrication of Si Heterojunction Solar Cells. *Nano Lett.* **2016**, *16*, 1925–1932. [CrossRef] [PubMed]
79. Yang, X.; Bi, Q.; Ali, H.; Davis, K.; Schoenfeld, W.V.; Weber, K. High-Performance TiO_2-Based Electron-Selective Contacts for Crystalline Silicon Solar Cells. *Adv. Mater.* **2016**, *28*, 5891–5897. [CrossRef] [PubMed]
80. Woods-Robinson, R.; Cooper, J.K.; Xu, X.; Schelhas, L.T.; Pool, V.L.; Faghaninia, A.; Lo, C.S.; Toney, M.F.; Sharp, I.D.; Ager III, J.W. P-type transparent Cu-alloyed ZnS deposited at room temperature. *Adv. Electron. Mater.* **2016**, *2*, 1500396. [CrossRef]
81. Maurya, S.K.; Liu, Y.; Xu, X.; Woods-Robinson, R.; Das, C.; Ager, J.W.; Balasubramaniam, K. High figure-of-merit p-type transparent conductor, Cu alloyed ZnS via radio frequency magnetron sputtering. *J. Phys. D Appl. Phys.* **2017**, *50*, 505107. [CrossRef]
82. Mahuli, N.; Saha, D.; Maurya, S.K.; Sinha, S.; Patra, N.; Kavaipatti, B.; Sarkar, S.K. Atomic layer deposition of transparent and conducting p-type Cu(I)incorporated ZnS thin films: Unravelling the role of compositional heterogeneity on optical and carrier transport properties. *J. Phys. Chem. C* **2018**, *122*, 16356–16367. [CrossRef]
83. Woods-Robinson, R.; Ablekim, T.; Norman, A.; Johnston, S.; Persson, K.A.; Reese, M.O.; Metzger, W.K.; Zakutayev, A. Sputtered p-Type $Cu_xZn_{1-x}S$ Back Contact to CdTe Solar Cells. *ACS Appl. Energy Mater.* **2020**, *3*, 5427–5438. [CrossRef]
84. Liu, M.L.; Huang, F.Q.; Chen, L.D.; Wang, Y.M.; Wang, Y.H.; Li, G.F.; Zhang, Q. p-type transparent conductor: Zn-doped $CuAlS_2$. *Appl. Phys. Lett.* **2007**, *90*, 2109. [CrossRef]
85. Park, S.; Keszler, D.A.; Valencia, M.M.; Hoffman, R.L.; Bender, J.P.; Wager, J.F. Transparent p-type conducting $BaCu_2S_2$ films. *Appl. Phys. Lett.* **2002**, *80*, 4393–4394. [CrossRef]
86. Yanagi, H.; Tate, J.; Park, S.; Park, C.H.; Keszler, D.A. p-Type conductivity in wide-band-gap BaCuQF (Q = S, Se). *Appl. Phys. Lett.* **2003**, *82*, 2814–2816. [CrossRef]
87. Ruttanapun, C.; Prachamon, W.; Wichainchai, A. Optoelectronic properties of $Cu_{1-x}Pt_xFeO_2$ ($0 \leq x \leq 0.05$) delafossite for p-type transparent conducting oxide. *Curr. Appl. Phys.* **2012**, *12*, 166–170. [CrossRef]
88. Manoj, R.; Nisha, M.; Vanaja, K.; Jayaraj, M. Effect of oxygen intercalation on properties of sputtered $CuYO_2$ for potential use as p-type transparent conducting films. *Bull. Mater. Sci.* **2008**, *31*, 49–53. [CrossRef]
89. Yang, C.; Kneiβ, M.; Lorenz, M.; Grundmann, M. Room-temperature synthesized copper iodide thin film as degenerate p-type transparent conductor with a boosted figure of merit. *Proc. Natl. Acad. Sci. USA* **2016**, *113*, 12929–12933. [CrossRef]
90. Windisch, C., Jr.; Exarhos, G.J.; Ferris, K.F.; Engelhard, M.H.; Stewart, D.C. Infrared transparent spinel films with p-type conductivity. *Thin Solid Film.* **2001**, *398*, 45–52. [CrossRef]
91. Windisch, C.F., Jr.; Ferris, K.F.; Exarhos, G.J. Synthesis and characterization of transparent conducting oxide cobalt-nickel spinel films. *J. Vac. Sci. Technol. Vacuum Surfaces Film.* **2001**, *19*, 1647–1651. [CrossRef]
92. Chen, H.Y.; Su, H.C.; Chen, C.H.; Liu, K.L.; Tsai, C.M.; Yen, S.J.; Yew, T.R. Indium-doped molybdenum oxide as a new p-type transparent conductive oxide. *J. Mater. Chem.* **2011**, *21*, 5745–5752. [CrossRef]

93. Kamioka, H.; Hiramatsu, H.; Ohta, H.; Hirano, M.; Ueda, K.; Kamiya, T.; Hosono, H. Third-order optical nonlinearity originating from room-temperature exciton in layered compounds LaCuOS and LaCuOSe. *Appl. Phys. Lett.* **2004**, *84*, 879–881. [CrossRef]
94. Zhang, K.H.; Du, Y.; Papadogianni, A.; Bierwagen, O.; Sallis, S.; Piper, L.F.; Bowden, M.E.; Shutthanandan, V.; Sushko, P.V.; Chambers, S.A. Perovskite Sr-Doped $LaCrO_3$ as a New p-Type Transparent Conducting Oxide. *Adv. Mater.* **2015**, *27*, 5191–5195. [CrossRef]
95. Bian, J.; Li, X.; Gao, X.; Yu, W.; Chen, L. Deposition and electrical properties of N-In codoped p-type ZnO films by ultrasonic spray pyrolysis. *Appl. Phys. Lett.* **2004**, *84*, 541–543. [CrossRef]
96. Hui, K.; Hui, K.S.; Li, L.; Cho, Y.; Singh, J. Low resistivity p-type $Zn_{1-x}Al_xO$:Cu_2O composite transparent conducting oxide thin film fabricated by sol-gel method. *Mater. Res. Bull.* **2013**, *48*, 96–100. [CrossRef]
97. Narushima, S.; Mizoguchi, H.; Shimizu, K.i.; Ueda, K.; Ohta, H.; Hirano, M.; Kamiya, T.; Hosono, H. A p-type amorphous oxide semiconductor and room temperature fabrication of amorphous oxide p–n heterojunction diodes. *Adv. Mater.* **2003**, *15*, 1409–1413. [CrossRef]
98. Kim, S.; Cianfrone, J.; Sadik, P.; Kim, K.W.; Ivill, M.; Norton, D. Room temperature deposited oxide pn junction using p-type zinc-cobalt-oxide. *J. Appl. Phys.* **2010**, *107*, 103538. [CrossRef]
99. Huang, F.Q.; Liu, M.L.; Yang, C. Highly enhanced p-type electrical conduction in wide band gap $Cu_{1+x}Al_{1-x}S_2$ polycrystals. *Sol. Energy Mater. Sol. Cells* **2011**, *95*, 2924–2927. [CrossRef]
100. Banerjee, S.; Dan, A.; Chakravorty, D. Review synthesis of conducting nanowires. *J. Mater. Sci.* **2002**, *37*, 4261–4271. [CrossRef]
101. Ye, S.; Stewart, I.E.; Chen, Z.; Li, B.; Rathmell, A.R.; Wiley, B.J. How copper nanowires grow and how to control their properties. *Acc. Chem. Res.* **2016**, *49*, 442–451. [CrossRef]
102. Ahn, J.; Hwang, H.; Jeong, S.; Moon, J. Metal-Nanowire-Electrode-Based Perovskite Solar Cells: Challenging Issues and New Opportunities. *Adv. Energy Mater.* **2017**, *7*, 1602751. [CrossRef]
103. Nam, V.B.; Lee, D. Copper nanowires and their applications for flexible, transparent conducting films: A review. *Nanomaterials* **2016**, *6*, 47. [CrossRef] [PubMed]
104. Langley, D.; Giusti, G.; Mayousse, C.; Celle, C.; Bellet, D.; Simonato, J.P. Flexible transparent conductive materials based on silver nanowire networks: A review. *Nanotechnology* **2013**, *24*, 452001. [CrossRef]
105. Soukoulis, C.M.; Wegener, M. Past achievements and future challenges in the development of three-dimensional photonic metamaterials. *Nat. Photonics* **2011**, *5*, 523–530. [CrossRef]
106. Reuteler, J.; Hütter, M.; Gauckler, L.J. Backbone of conductivity in two-dimensional metal-insulator composites. *J. Appl. Phys.* **2011**, *110*, 024909. [CrossRef]
107. Kumar, A.; Kulkarni, G. Evaluating conducting network based transparent electrodes from geometrical considerations. *J. Appl. Phys.* **2016**, *119*, 015102. [CrossRef]
108. Preston, C.; Xu, Y.; Han, X.; Munday, J.N.; Hu, L. Optical haze of transparent and conductive silver nanowire films. *Nano Res.* **2013**, *6*, 461–468. [CrossRef]
109. Bellet, D.; Lagrange, M.; Sannicolo, T.; Aghazadehchors, S.; Nguyen, V.H.; Langley, D.P.; Muñoz-Rojas, D.; Jiménez, C.; Bréchet, Y.; Nguyen, N.D. Transparent electrodes based on silver nanowire networks: From physical considerations towards device integration. *Materials* **2017**, *10*, 570. [CrossRef] [PubMed]
110. Lagrange, M.; Langley, D.; Giusti, G.; Jiménez, C.; Bréchet, Y.; Bellet, D. Optimization of silver nanowire-based transparent electrodes: Effects of density, size and thermal annealing. *Nanoscale* **2015**, *7*, 17410–17423. [CrossRef]
111. Mutiso, R.M.; Sherrott, M.C.; Rathmell, A.R.; Wiley, B.J.; Winey, K.I. Integrating simulations and experiments to predict sheet resistance and optical transmittance in nanowire films for transparent conductors. *ACS Nano* **2013**, *7*, 7654–7663. [CrossRef]
112. Kang, H.; Yi, G.R.; Kim, Y.J.; Cho, J.H. Junction welding techniques for metal nanowire network electrodes. *Macromol. Res.* **2018**, *26*, 1066–1073. [CrossRef]
113. Ding, Y.; Cui, Y.; Liu, X.; Liu, G.; Shan, F. Welded silver nanowire networks as high-performance transparent conductive electrodes: Welding techniques and device applications. *Appl. Mater. Today* **2020**, *20*, 100634. [CrossRef]
114. Lu, Y.; Huang, J.Y.; Wang, C.; Sun, S.; Lou, J. Cold welding of ultrathin gold nanowires. *Nat. Nanotechnol.* **2010**, *5*, 218–224. [CrossRef]
115. Hwang, B.; Shin, H.A.S.; Kim, T.; Joo, Y.C.; Han, S.M. Highly reliable Ag nanowire flexible transparent electrode with mechanically welded junctions. *Small* **2014**, *10*, 3397–3404. [CrossRef] [PubMed]
116. Green, M.A. Thin-film solar cells: Review of materials, technologies and commercial status. *J. Mater. Sci. Mater. Electron.* **2007**, *18*, 15–19. [CrossRef]
117. Hegedus, S.S.; Shafarman, W.N. Thin-film solar cells: Device measurements and analysis. *Prog. Photovoltaics Res. Appl.* **2004**, *12*, 155–176. [CrossRef]
118. Angmo, D.; Krebs, F.C. Flexible ITO-free polymer solar cells. *J. Appl. Polym. Sci.* **2013**, *129*, 1–14. [CrossRef]
119. Basarir, F.; Irani, F.S.; Kosemen, A.; Camic, B.T.; Oytun, F.; Tunaboylu, B.; Shin, H.J.; Nam, K.Y.; Choi, H. Recent progresses on solution-processed silver nanowire based transparent conducting electrodes for organic solar cells. *Mater. Today Chem.* **2017**, *3*, 60–72. [CrossRef]
120. Lim, J.W.; Cho, D.Y.; Kim, J.; Na, S.I.; Kim, H.K. Simple brush-painting of flexible and transparent Ag nanowire network electrodes as an alternative ITO anode for cost-efficient flexible organic solar cells. *Sol. Energy Mater. Sol. Cells* **2012**, *107*, 348–354. [CrossRef]

121. Gaynor, W.; Burkhard, G.F.; McGehee, M.D.; Peumans, P. Smooth nanowire/polymer composite transparent electrodes. *Adv. Mater.* **2011**, *23*, 2905–2910. [CrossRef]
122. Andrés, L.J.; Menéndez, M.F.; Gómez, D.; Martínez, A.L.; Bristow, N.; Kettle, J.P.; Menéndez, A.; Ruiz, B. Rapid synthesis of ultra-long silver nanowires for tailor-made transparent conductive electrodes: Proof of concept in organic solar cells. *Nanotechnology* **2015**, *26*, 265201. [CrossRef]
123. Chen, S.; Cui, Q.; Guo, X. Annealing-free solution-processed silver nanowire-polymer composite transparent electrodes and flexible device applications. *IEEE Trans. Nanotechnol.* **2014**, *14*, 36–41. [CrossRef]
124. Sun, J.; Jasieniak, J. Semi-transparent solar cells. *J. Phys. D Appl. Phys.* **2017**, *50*, 093001. [CrossRef]
125. Hu, Z.; Wang, J.; Ma, X.; Gao, J.; Xu, C.; Yang, K.; Wang, Z.; Zhang, J.; Zhang, F. A critical review on semitransparent organic solar cells. *Nano Energy* **2020**, *78*, 105376. [CrossRef]
126. Tai, Q.; Yan, F. Emerging semitransparent solar cells: Materials and device design. *Adv. Mater.* **2017**, *29*, 1700192. [CrossRef]
127. Eperon, G.E.; Burlakov, V.M.; Goriely, A.; Snaith, H.J. Neutral color semitransparent microstructured perovskite solar cells. *ACS Nano* **2014**, *8*, 591–598. [CrossRef] [PubMed]
128. Guo, F.; Azimi, H.; Hou, Y.; Przybilla, T.; Hu, M.; Bronnbauer, C.; Langner, S.; Spiecker, E.; Forberich, K.; Brabec, C.J. High-performance semitransparent perovskite solar cells with solution-processed silver nanowires as top electrodes. *Nanoscale* **2015**, *7*, 1642–1649. [CrossRef] [PubMed]
129. Dai, X.; Zhang, Y.; Shen, H.; Luo, Q.; Zhao, X.; Li, J.; Lin, H. Working from both sides: Composite metallic semitransparent top electrode for high performance perovskite solar cells. *ACS Appl. Mater. Interfaces* **2016**, *8*, 4523–4531. [CrossRef]
130. Leijtens, T.; Eperon, G.E.; Pathak, S.; Abate, A.; Lee, M.M.; Snaith, H.J. Overcoming ultraviolet light instability of sensitized TiO_2 with meso-superstructured organometal tri-halide perovskite solar cells. *Nat. Commun.* **2013**, *4*, 1–8. [CrossRef]
131. Kim, A.; Lee, H.; Kwon, H.C.; Jung, H.S.; Park, N.G.; Jeong, S.; Moon, J. Fully solution-processed transparent electrodes based on silver nanowire composites for perovskite solar cells. *Nanoscale* **2016**, *8*, 6308–6316. [CrossRef]
132. Im, H.G.; Jeong, S.; Jin, J.; Lee, J.; Youn, D.Y.; Koo, W.T.; Kang, S.B.; Kim, H.J.; Jang, J.; Lee, D.; et al. Hybrid crystalline-ITO/metal nanowire mesh transparent electrodes and their application for highly flexible perovskite solar cells. *NPG Asia Mater.* **2016**, *8*, e282. [CrossRef]
133. Fukuda, K.; Yu, K.; Someya, T. The future of flexible organic solar cells. *Adv. Energy Mater.* **2020**, *10*, 2000765. [CrossRef]
134. Li, X.; Li, P.; Wu, Z.; Luo, D.; Yu, H.Y.; Lu, Z.H. Review and perspective of materials for flexible solar cells. *Mater. Rep. Energy* **2021**, *1*, 100001. [CrossRef]
135. Pagliaro, M.; Ciriminna, R.; Palmisano, G. Flexible solar cells. *ChemSusChem Chem. Sustain. Energy Mater.* **2008**, *1*, 880–891.
136. Feng, J. Mechanical properties of hybrid organic-inorganic CH3NH3BX3 (B = Sn, Pb; X = Br, I) perovskites for solar cell absorbers. *Apl Mater.* **2014**, *2*, 081801. [CrossRef]
137. Rakita, Y.; Cohen, S.R.; Kedem, N.K.; Hodes, G.; Cahen, D. Mechanical properties of $APbX_3$ (A = Cs or CH_3NH_3; X = I or Br) perovskite single crystals. *MRS Commun.* **2015**, *5*, 623–629. [CrossRef]
138. Sun, S.; Fang, Y.; Kieslich, G.; White, T.J.; Cheetham, A.K. Mechanical properties of organic–inorganic halide perovskites, $CH_3NH_3PbX_3$ (X = I, Br and Cl), by nanoindentation. *J. Mater. Chem. A* **2015**, *3*, 18450–18455. [CrossRef]
139. Luo, S.; Lee, J.H.; Liu, C.W.; Shieh, J.M.; Shen, C.H.; Wu, T.T.; Jang, D.; Greer, J.R. Strength, stiffness, and microstructure of $Cu(In,Ga)Se_2$ thin films deposited via sputtering and co-evaporation. *Appl. Phys. Lett.* **2014**, *105*, 011907. [CrossRef]
140. Grillo, S.; Ducarroir, M.; Nadal, M.; Tournie, E.; Faurie, J. Nanoindentation of Si, GaP, GaAs and ZnSe single crystals. *J. Phys. D Appl. Phys.* **2002**, *36*, L5. [CrossRef]
141. Zardetto, V.; Brown, T.M.; Reale, A.; Di Carlo, A. Substrates for flexible electronics: A practical investigation on the electrical, film flexibility, optical, temperature, and solvent resistance properties. *J. Polym. Sci. Part B Polym. Phys.* **2011**, *49*, 638–648. [CrossRef]
142. Zou, D.; Wang, D.; Chu, Z.; Lv, Z.; Fan, X. Fiber-shaped flexible solar cells. *Coord. Chem. Rev.* **2010**, *254*, 1169–1178. [CrossRef]
143. Hauger, T.C.; Al-Rafia, S.I.; Buriak, J.M. Rolling silver nanowire electrodes: Simultaneously addressing adhesion, roughness, and conductivity. *ACS Appl. Mater. Interfaces* **2013**, *5*, 12663–12671. [CrossRef]
144. Hosseinzadeh Khaligh, H.; Goldthorpe, I.A. Hot-rolling nanowire transparent electrodes for surface roughness minimization. *Nanoscale Res. Lett.* **2014**, *9*, 1–5. [CrossRef]
145. Cheng, T.; Zhang, Y.Z.; Yi, J.P.; Yang, L.; Zhang, J.D.; Lai, W.Y.; Huang, W. Inkjet-printed flexible, transparent and aesthetic energy storage devices based on PEDOT: PSS/Ag grid electrodes. *J. Mater. Chem. A* **2016**, *4*, 13754–13763. [CrossRef]
146. Kim, S.; Lee, S.J.; Cho, S.; Shin, S.; Jeong, U; Myoung, J.-M. Improved stability of transparent PEDOT:PSS/Ag nanowire hybrid electrodes by using non-ionic surfactants. *Chem. Commun.* **2017**, *53*, 8292–8295.
147. Langley, D.; Lagrange, M.; Giusti, G.; Jiménez, C.; Bréchet, Y.; Nguyen, N.D.; Bellet, D. Metallic nanowire networks: Effects of thermal annealing on electrical resistance. *Nanoscale* **2014**, *6*, 13535–13543. [CrossRef] [PubMed]
148. Lee, M.; Ko, Y.; Min, B.K.; Jun, Y. Silver nanowire top electrodes in flexible perovskite solar cells using titanium metal as substrate. *ChemSusChem* **2016**, *9*, 31–35. [CrossRef] [PubMed]
149. Liang, Z.; Graham, K.R. Surface modification of silver nanowires for morphology and processing control in composite transparent electrodes. *ACS Appl. Mater. Interfaces* **2015**, *7*, 21652–21656. [CrossRef]
150. Fan, Z.; Du, D.; Yao, H.; Ouyang, J. Higher PEDOT molecular weight giving rise to higher thermoelectric property of PEDOT: PSS: A comparative study of clevios P and clevios PH1000. *ACS Appl. Mater. Interfaces* **2017**, *9*, 11732–11738. [CrossRef]

151. Huseynova, G.; Hyun Kim, Y.; Lee, J.H.; Lee, J. Rising advancements in the application of PEDOT:PSS as a prosperous transparent and flexible electrode material for solution-processed organic electronics. *J. Inf. Disp.* **2020**, *21*, 71–91. [CrossRef]
152. Nardes, A.M.; Kemerink, M.; De Kok, M.; Vinken, E.; Maturova, K.; Janssen, R. Conductivity, work function, and environmental stability of PEDOT:PSS thin films treated with sorbitol. *Org. Electron.* **2008**, *9*, 727–734. [CrossRef]
153. Gueye, M.N.; Carella, A.; Massonnet, N.; Yvenou, E.; Brenet, S.; Faure-Vincent, J.; Pouget, S.; Rieutord, F.; Okuno, H.; Benayad, A.; et al. Structure and dopant engineering in PEDOT thin films: Practical tools for a dramatic conductivity enhancement. *Chem. Mater.* **2016**, *28*, 3462–3468. [CrossRef]
154. Oh, S.H.; Heo, S.J.; Yang, J.S.; Kim, H.J. Effects of ZnO nanoparticles on P3HT:PCBM organic solar cells with DMF-modulated PEDOT:PSS buffer layers. *ACS Appl. Mater. Interfaces* **2013**, *5*, 11530–11534. [CrossRef]
155. Yildirim, E.; Wu, G.; Yong, X.; Tan, T.L.; Zhu, Q.; Xu, J.; Ouyang, J.; Wang, J.S.; Yang, S.W. A theoretical mechanistic study on electrical conductivity enhancement of DMSO treated PEDOT:PSS. *J. Mater. Chem. C* **2018**, *6*, 5122–5131. [CrossRef]
156. Cruz-Cruz, I.; Reyes-Reyes, M.; Aguilar-Frutis, M.A.; Rodriguez, A.; López-Sandoval, R. Study of the effect of DMSO concentration on the thickness of the PSS insulating barrier in PEDOT:PSS thin films. *Synth. Met.* **2010**, *160*, 1501–1506. [CrossRef]
157. Lin, Y.J.; Ni, W.S.; Lee, J.Y. Effect of incorporation of ethylene glycol into PEDOT:PSS on electron phonon coupling and conductivity. *J. Appl. Phys.* **2015**, *117*, 215501.
158. Bießmann, L.; Saxena, N.; Hohn, N.; Hossain, M.A.; Veinot, J.G.; Müller-Buschbaum, P. Highly conducting, transparent PEDOT:PSS polymer electrodes from post-treatment with weak and strong acids. *Adv. Electron. Mater.* **2019**, *5*, 1800654. [CrossRef]
159. Lee, J.H.; Jeong, Y.R.; Lee, G.; Jin, S.W.; Lee, Y.H.; Hong, S.Y.; Park, H.; Kim, J.W.; Lee, S.S.; Ha, J.S. Highly conductive, stretchable, and transparent PEDOT:PSS electrodes fabricated with triblock copolymer additives and acid treatment. *ACS Appl. Mater. Interfaces* **2018**, *10*, 28027–28035. [CrossRef] [PubMed]
160. Fang, G.; Wu, S.; Xie, Z.; Geng, Y.; Wang, L. Enhanced Performance for Polymer Solar Cells by Using Surfactant-Modified PEDOT:PSS as the Anode Buffer Layer. *Macromol. Chem. Phys.* **2011**, *212*, 1846–1851. [CrossRef]
161. Zhu, Y.; Wang, S.; Ma, R.; Wang, C. The improvement of inverted perovskite solar cells by the introduction of CTAB into PEDOT:PSS. *Sol. Energy* **2019**, *188*, 28–34. [CrossRef]
162. Fan, P.; Zheng, D.; Zheng, Y.; Yu, J. Efficient and stable planar pin perovskite solar cells by doping tungsten compound into PEDOT:PSS to facilitate perovskite crystalline. *Electrochim. Acta* **2018**, *283*, 922–930. [CrossRef]
163. Syed, A.A.; Poon, C.Y.; Li, H.W.; Zhu, F. A sodium citrate-modified-PEDOT:PSS hole transporting layer for performance enhancement in inverted planar perovskite solar cells. *J. Mater. Chem. C* **2019**, *7*, 5260–5266. [CrossRef]
164. Hu, L.; Sun, K.; Wang, M.; Chen, W.; Yang, B.; Fu, J.; Xiong, Z.; Li, X.; Tang, X.; Zang, Z.; et al. Inverted planar perovskite solar cells with a high fill factor and negligible hysteresis by the dual effect of NaCl-doped PEDOT:PSS. *ACS Appl. Mater. Interfaces* **2017**, *9*, 43902–43909. [CrossRef]
165. Liu, X.; Li, B.; Zhang, N.; Yu, Z.; Sun, K.; Tang, B.; Shi, D.; Yao, H.; Ouyang, J.; Gong, H. Multifunctional RbCl dopants for efficient inverted planar perovskite solar cell with ultra-high fill factor, negligible hysteresis and improved stability. *Nano Energy* **2018**, *53*, 567–578. [CrossRef]
166. Lim, J.E.; Lee, S.M.; Kim, S.S.; Kim, T.W.; Koo, H.W.; Kim, H.K. Brush-paintable and highly stretchable Ag nanowire and PEDOT:PSS hybrid electrodes. *Sci. Rep.* **2017**, *7*, 1–12. [CrossRef] [PubMed]
167. Liu, Y.s.; Feng, J.; Ou, X.L.; Cui, H.f.; Xu, M.; Sun, H.B. Ultrasmooth, highly conductive and transparent PEDOT:PSS/silver nanowire composite electrode for flexible organic light-emitting devices. *Org. Electron.* **2016**, *31*, 247–252. [CrossRef]
168. Park, Y.; Soon Choi, K.; Young Kim, S. Graphene oxide/PEDOT:PSS and reduced graphene oxide/PEDOT:PSS hole extraction layers in organic photovoltaic cells. *Phys. Status Solidi* **2012**, *209*, 1363–1368. [CrossRef]
169. Mahmoudi, T.; Wang, Y.; Hahn, Y.B. Graphene and its derivatives for solar cells application. *Nano Energy* **2018**, *47*, 51–65. [CrossRef]
170. Sung, H.; Ahn, N.; Jang, M.S.; Lee, J.K.; Yoon, H.; Park, N.G.; Choi, M. Transparent conductive oxide-free graphene-based perovskite solar cells with over 17% efficiency. *Adv. Energy Mater.* **2016**, *6*, 1501873. [CrossRef]
171. Kumar, S.; McEvoy, N.; Kim, H.Y.; Lee, K.; Peltekis, N.; Rezvani, E.; Nolan, H.; Weidlich, A.; Daly, R.; Duesberg, G.S. CVD growth and processing of graphene for electronic applications. *Phys. Status Solidi* **2011**, *248*, 2604–2608. [CrossRef]
172. Gomez De Arco, L.; Zhang, Y.; Schlenker, C.W.; Ryu, K.; Thompson, M.E.; Zhou, C. Continuous, highly flexible, and transparent graphene films by chemical vapor deposition for organic photovoltaics. *ACS Nano* **2010**, *4*, 2865–2873. [CrossRef]
173. De Arco, L.G.; Zhang, Y.; Kumar, A.; Zhou, C. Synthesis, transfer, and devices of single-and few-layer graphene by chemical vapor deposition. *IEEE Trans. Nanotechnol.* **2009**, *8*, 135–138. [CrossRef]
174. Ball, J.M.; Lee, M.M.; Hey, A.; Snaith, H.J. Low-temperature processed meso-superstructured to thin-film perovskite solar cells. *Energy Environ. Sci.* **2013**, *6*, 1739–1743. [CrossRef]
175. Ramuz, M.P.; Vosgueritchian, M.; Wei, P.; Wang, C.; Gao, Y.; Wu, Y.; Chen, Y.; Bao, Z. Evaluation of solution-processable carbon-based electrodes for all-carbon solar cells. *ACS Nano* **2012**, *6*, 10384–10395. [CrossRef] [PubMed]
176. You, P.; Liu, Z.; Tai, Q.; Liu, S.; Yan, F. Efficient semitransparent perovskite solar cells with graphene electrodes. *Adv. Mater.* **2015**, *27*, 3632–3638. [CrossRef] [PubMed]
177. Lee, Y.J.; Seo, Y.I.; Kim, S.H.; Kim, D.G.; Kim, Y.D. Optical properties of molybdenum oxide thin films deposited by chemical vapor transport of $MoO_3(OH)_2$. *Appl. Phys. A* **2009**, *97*, 237–241. [CrossRef]

178. Wang, X.; Li, Z.; Xu, W.; Kulkarni, S.A.; Batabyal, S.K.; Zhang, S.; Cao, A.; Wong, L.H. TiO_2 nanotube arrays based flexible perovskite solar cells with transparent carbon nanotube electrode. *Nano Energy* **2015**, *11*, 728–735. [CrossRef]
179. Li, Z.; Jia, Y.; Wei, J.; Wang, K.; Shu, Q.; Gui, X.; Zhu, H.; Cao, A.; Wu, D. Large area, highly transparent carbon nanotube spiderwebs for energy harvesting. *J. Mater. Chem.* **2010**, *20*, 7236–7240. [CrossRef]
180. Jeon, I.; Yoon, J.; Ahn, N.; Atwa, M.; Delacou, C.; Anisimov, A.; Kauppinen, E.I.; Choi, M.; Maruyama, S.; Matsuo, Y. Carbon nanotubes versus graphene as flexible transparent electrodes in inverted perovskite solar cells. *J. Phys. Chem. Lett.* **2017**, *8*, 5395–5401. [CrossRef]
181. Imazu, N.; Fujigaya, T.; Nakashima, N. Fabrication of highly transparent, thermally stable, and scalable conductive films from double-walled carbon nanotubes. *Bull. Chem. Soc. Jpn.* **2015**, *88*, 217–221. [CrossRef]
182. Hecht, D.S.; Hu, L.; Irvin, G. Emerging transparent electrodes based on thin films of carbon nanotubes, graphene, and metallic nanostructures. *Adv. Mater.* **2011**, *23*, 1482–1513. [CrossRef]
183. Duclaux, L. Review of the doping of carbon nanotubes (multiwalled and single-walled). *Carbon* **2002**, *40*, 1751–1764. [CrossRef]
184. Geng, H.Z.; Kim, K.K.; Song, C.; Xuyen, N.T.; Kim, S.M.; Park, K.A.; Lee, D.S.; An, K.H.; Lee, Y.S.; Chang, Y.; et al. Doping and de-doping of carbon nanotube transparent conducting films by dispersant and chemical treatment. *J. Mater. Chem.* **2008**, *18*, 1261–1266. [CrossRef]
185. Takenobu, T.; Kanbara, T.; Akima, N.; Takahashi, T.; Shiraishi, M.; Tsukagoshi, K.; Kataura, H.; Aoyagi, Y.; Iwasa, Y. Control of carrier density by a solution method in carbon-nanotube devices. *Adv. Mater.* **2005**, *17*, 2430–2434. [CrossRef]
186. Lee, R.; Kim, H.; Fischer, J.; Thess, A.; Smalley, R.E. Conductivity enhancement in single-walled carbon nanotube bundles doped with K and Br. *Nature* **1997**, *388*, 255–257. [CrossRef]
187. Skakalova, V.; Kaiser, A.; Dettlaff-Weglikowska, U.; Hrncarikova, K.; Roth, S. Effect of chemical treatment on electrical conductivity, infrared absorption, and Raman spectra of single-walled carbon nanotubes. *J. Phys. Chem. B* **2005**, *109*, 7174–7181. [CrossRef] [PubMed]
188. Zhang, J.; Gao, L.; Sun, J.; Liu, Y.; Wang, Y.; Wang, J.; Kajiura, H.; Li, Y.; Noda, K. Dispersion of single-walled carbon nanotubes by nafion in water/ethanol for preparing transparent conducting films. *J. Phys. Chem. C* **2008**, *112*, 16370–16376. [CrossRef]
189. Jeon, I.; Yoon, J.; Kim, U.; Lee, C.; Xiang, R.; Shawky, A.; Xi, J.; Byeon, J.; Lee, H.M.; Choi, M.; et al. High-performance solution-processed double-walled carbon nanotube transparent electrode for perovskite solar cells. *Adv. Energy Mater.* **2019**, *9*, 1901204. [CrossRef]
190. Jeon, I.; Matsuo, Y.; Maruyama, S. Single-walled carbon nanotubes in solar cells. In *Single-Walled Carbon Nanotubes*; Springer: New York, NY, USA, 2019; pp. 271–298.
191. Wang, Y.; Tong, S.W.; Xu, X.F.; Özyilmaz, B.; Loh, K.P. Interface engineering of layer-by-layer stacked graphene anodes for high-performance organic solar cells. *Adv. Mater.* **2011**, *23*, 1514–1518. [CrossRef] [PubMed]
192. Lang, F.; Gluba, M.A.; Albrecht, S.; Rappich, J.; Korte, L.; Rech, B.; Nickel, N.H. Perovskite solar cells with large-area CVD-graphene for tandem solar cells. *J. Phys. Chem. Lett.* **2015**, *6*, 2745–2750. [CrossRef] [PubMed]
193. Heo, J.H.; Shin, D.H.; Jang, M.H.; Lee, M.L.; Kang, M.G.; Im, S.H. Highly flexible, high-performance perovskite solar cells with adhesion promoted AuCl 3-doped graphene electrodes. *J. Mater. Chem. A* **2017**, *5*, 21146–21152. [CrossRef]
194. Jeon, I.; Chiba, T.; Delacou, C.; Guo, Y.; Kaskela, A.; Reynaud, O.; Kauppinen, E.I.; Maruyama, S.; Matsuo, Y. Single-walled carbon nanotube film as electrode in indium-free planar heterojunction perovskite solar cells: Investigation of electron-blocking layers and dopants. *Nano Lett.* **2015**, *15*, 6665–6671. [CrossRef]
195. Aitola, K.; Sveinbjörnsson, K.; Correa-Baena, J.P.; Kaskela, A.; Abate, A.; Tian, Y.; Johansson, E.M.; Grätzel, M.; Kauppinen, E.I.; Hagfeldt, A.; et al. Carbon nanotube-based hybrid hole-transporting material and selective contact for high efficiency perovskite solar cells. *Energy Environ. Sci.* **2016**, *9*, 461–466. [CrossRef]